*Advanced High-Explosive Flux
Compression Generator Development:
The CN-III Series*

*Bruce L. Freeman
Maurice G. Sheppard
C. Max Fowler*

MASTER

ADVANCED HIGH-EXPLOSIVE FLUX COMPRESSION GENERATOR DEVELOPMENT: THE CN-III SERIES

by

Bruce L. Freeman, Maurice G. Sheppard, and C. Max Fowler

ABSTRACT

A very successful series of three flux compression generator (FCG) experiments and one hydro-only test, designed to quantify the performance capabilities and limitations of high-current, high-field, high-power coaxial FCGs, is reported. In the last test, the CN-III FCG produced a peak current of >150 MA with a final doubling time of <10 μs into a 2-nH inductive load. Experimental results are in excellent agreement with extensive preshot and postshot one-dimensional (1D) and two-dimensional (2D) magnetohydrodynamic (MHD) calculations.

I. INTRODUCTION

Physics experiments and applications under extreme conditions of material density, energy density, temperature, pressure, and radiation require both special handling and a significant source of primary power. Most of these experiments involve the creation of plasmas, either as the main focus of the process, or as a by-product of the existing conditions. Many of these experiments conducted by Los Alamos National Laboratory (LANL) must be performed underground at the Nevada Test Site because of the extreme energy and power-density requirements. Given a reliable and flexible source of high-current, high-power, and high-energy electrical power, a significant fraction of these experiments and applications could be carried out more cheaply and easily above ground, without the use of nuclear sources.

Several large pulsed power facilities exist that fulfill some of these special requirements. However, these facilities are neither portable nor easily adaptable as particular experimental and programmatic requirements evolve. Another source of electrical power that fills in the gap left by conventional pulsed power machines is the high-explosive-driven flux compression

generator (FCG). Because of its flexibility and relatively inexpensive per-generator cost, the FCG is an ideal power supply when

1. portable pulsed power supplies are needed and repetition rates of no higher than a few shots per week are adequate,

2. experiments or applications involving new concepts or feasibility questions imply that pulsed power requirements are likely to evolve quickly as an experimental program progresses, and

3. extremely large electrical power outputs are required.

The FCG is probably not the best choice of power supplies if more than a few shots per week are needed and/or thousands of similar experiments with relatively minor parameter variations are required.

Practical generator design involves tradeoffs between current gain, peak output currents, current risetime, energy and power output, effective driving impedance required for various loads, and operation efficiency. Considerations of total FCG mass and high-explosive (HE) mass can also be important for certain applications. One of the key motivations for this series was to better define these tradeoffs, quantitatively. These experiments were also designed to explore the ultimate capabilities and limitations of FCGs and to define the current state-of-the-art for FCG technology.

In this study we adopted the following specific set of goals for a series of advanced FCG development experiments that would challenge the limits of traditional US FCG operating regimes:

1. Generate a 150-MA current pulse with a risetime of 10 μs or less using an existing HE initiation system. This current exceeds any FCG peak current produced outside of the Soviet Union.

2. Test and challenge the prevailing rule-of-thumb that limits the linear current density carried by an armature to about 1 MA/cm. A linear current density of 1 MA/cm is equivalent to a magnetic field of 1.3 MG at the armature-field interface.

3. Extract a reasonable fraction of the armature kinetic energy into magnetic field energy. This can be accomplished only by producing a high enough magnetic field so that the magnetic back-pressure will slow or even stop a portion of the armature before it collides with the stator. The goal here was not to achieve the best overall FCG efficiency in this development series, but to extract a high efficiency from some portion of the armature in a controlled and measurable fashion.

4. Calculate and model each test with 1D and 2D MHD computer codes to benchmark the codes and improve our understanding and predictive capability relative to FCG and high-magnetic-field physics.

To insure that our goals could be met, we adopted the philosophy that each test should be completely and carefully designed and calculated with the best tools available. These calculations were completed prior to each test and predictions concerning all aspects of FCG performance were available at shot time. Part of this process involved designing a series of experiments that were amenable to calculations. Three-dimensional (3D) and complex geometries were avoided. Each test was sufficiently diagnosed to permit meaningful and unambiguous comparisons with preshot calculations. Another aspect of our methodology was to allow enough time between experiments for complete postshot data analysis, follow-up calculations of the previous experiment, and new design calculations for the next experiment. On two occasions, the learning that accompanied one experiment was successfully incorporated into a modification of the next experiment to maximize the information return from the series. Finally, generator performance was first characterized in the traditional operating regime, and then it was pushed well beyond normal operating limits to challenge both rules-of-thumb and theory.

The experimental series was conducted with a coaxial FCG, denoted the CN-III, which was specifically designed with the above goals and methodology in mind. Four experiments were performed as part of the developmental series. The first test involved an armature case-motion test in the absence of magnetic fields. This test verified armature integrity and visually examined the dynamic, high-current joints between the armature and the end-wall glide planes. The second test was a low-current experiment to demonstrate the "small-signal gain" characteristics of the CN-III. This test operated in the traditional and "well understood" FCG regime in which the magnetic field pressure is not large enough to impede the hydrodynamic motion of the armature. The third test was an intermediate-current shot that was designed as an initial challenge of the generator's capabilities. This experiment was intended to reach a regime in which the magnetic field would be strong enough to slow the armature during the final stages of flux compression. Preshot results for this test were reported in a paper describing the calculational algorithm that was developed in the RAVEN code to handle these simulations.[1] The final test in the CN-III series was a high-current experiment that achieved the stated goals and performed as predicted. The last two tests were reported at the IEEE Plasma Science Conference.[2,3]

This series has given the US the capability to design high-efficiency, fast-risetime FCGs with peak currents in excess of 300 MA, usable output energies in excess of 500 MJ, and peak output powers in the 10s of TW. In deference to the explosive pulsed power effort in the Soviet Union, they have apparently possessed this capability for more than a decade, even though complete documentation of their accomplishments was unavailable until some time after the CN-III series was initiated.[4-7]

II. BASIC FCG OPERATION

HE-driven FCGs use flux conservation to convert the chemical energy of HE into magnetic field energy. When the HE in an FCG is detonated, its energy is deposited into kinetic energy of a moving conductor, called an armature. The kinetic energy of the armature is used to do work against a pre-existing magnetic field that is trapped between the armature and a stationary conductor, called the stator. As the gap between the armature and the stator is closed, the inductance of the FCG is reduced, the current is amplified, and the energy in the magnetic field is boosted. An excellent introduction to FCG operation is available in a LANL document prepared by Fowler, Caird, and Garn.[8]

To derive a simplified set of equations that illustrate the principles of FCG operation, consider a lossless FCG with a generator inductance, L_g, and load inductance, L_l. One can write the initial magnetic flux, Φ_0, as

$$\Phi_0 = (L_g + L_l)I_0 \quad,$$

where I_0 is an externally supplied seed-current that provides the initial trapped magnetic field. The magnetic field energy supplied by the seed-current is

$$E_0 = \frac{1}{2}(L_g + L_l)I_0^2 \quad.$$

During the flux compression process, the HE-driven armature wipes out the generator inductance, leaving only the load inductance at generator burnout. The final flux, which is all transferred to the load, is written

$$\Phi_f = L_l I_f \quad.$$

Assuming no resistive losses in an ideal FCG, flux conservation states

$$\Phi_0 = \Phi_f \quad.$$

Solving for the ideal current amplification factor gives

$$\frac{I_f}{I_0} = \frac{(L_g + L_l)}{L_l} \quad,$$

which is just the ratio of initial to final inductance. The ideal energy amplification factor is obtained by dividing the final magnetic energy,

$$E_f = \frac{1}{2}L_l I_f^2$$

by the initial seed field energy to give

$$\frac{E_f}{E_0} \quad \frac{I_f}{I_0} \quad .$$

Obviously, real FCGs have finite electrical conductivities and other loss mechanisms, and, therefore, do not operate with 100% magnetic flux conservation efficiency. Likewise, an implicit assumption in these equations is that the HE has sufficient energy to completely wipe out the generator inductance. One of the purposes of this study is to define and understand the limits to FCG performance, both calculationally and experimentally.

III. CN-III DESCRIPTION

A picture of the CN-III as tested in the low- and medium-current experiments is shown in Fig. 1. The original CN-III armature and glide plane design was tested in the case-motion experiment. Modifications that were suggested by the results of the case-motion experiment and postshot calculations are reflected in Fig.1. These changes will be discussed in detail with the description of the case-motion test. The high-current CN-III experiment incorporated additional modifications to the CN-III geometry, which will also be discussed later. The stator is a cylinder made from a single piece of spun-cast copper, weighing about 3400 kg (7500 lbs). The inner diameter of the stator ranges from 44.12 cm at the input end to 55.67 cm at the load-ring opening. The stator formed a 2.5° angle with the armature to assure phased flux compression and to minimize flux trapping and jetting along the armature-stator contact surface during generator operation.

The armature is a fully annealed, aluminum-6061 cylinder, with a 24.77-cm outside diameter, a wall thickness of 0.95 cm, a smooth inner-surface and a polished outer-surface finish. The finish on both the inside and the outside of the armature minimizes perturbations that could set up instabilities and also helps to control the ejection of fluff from the outside armature surface at shock breakout. The expansion ratio of the armature ranges from 1.78:1 at the input end to 2.25:1 at the load-ring opening.

Inside the armature is the HE charge, which is initiated simultaneously along 5/6 of its 144.12-cm length. The first 5/6 of the explosive system is composed of five Falcon modules, which are cylinders of PBX-9501, initiated simultaneously along the inside surface. The remaining 1/6 of the explosive system, a solid Falcon with no internal initiation mechanism, is detonated sympathetically from one end by the adjacent Falcon module. The detonation wave then propagates axially in the solid Falcon as in more traditional, end-initiated coaxial FCGs. The Falcon modules, each 24.02-cm long and 20.32 cm in diameter, are stacked and glued together before being inserted inside the armature tube. The simultaneous-to-propagating interface was specifically designed to minimize the current path length near
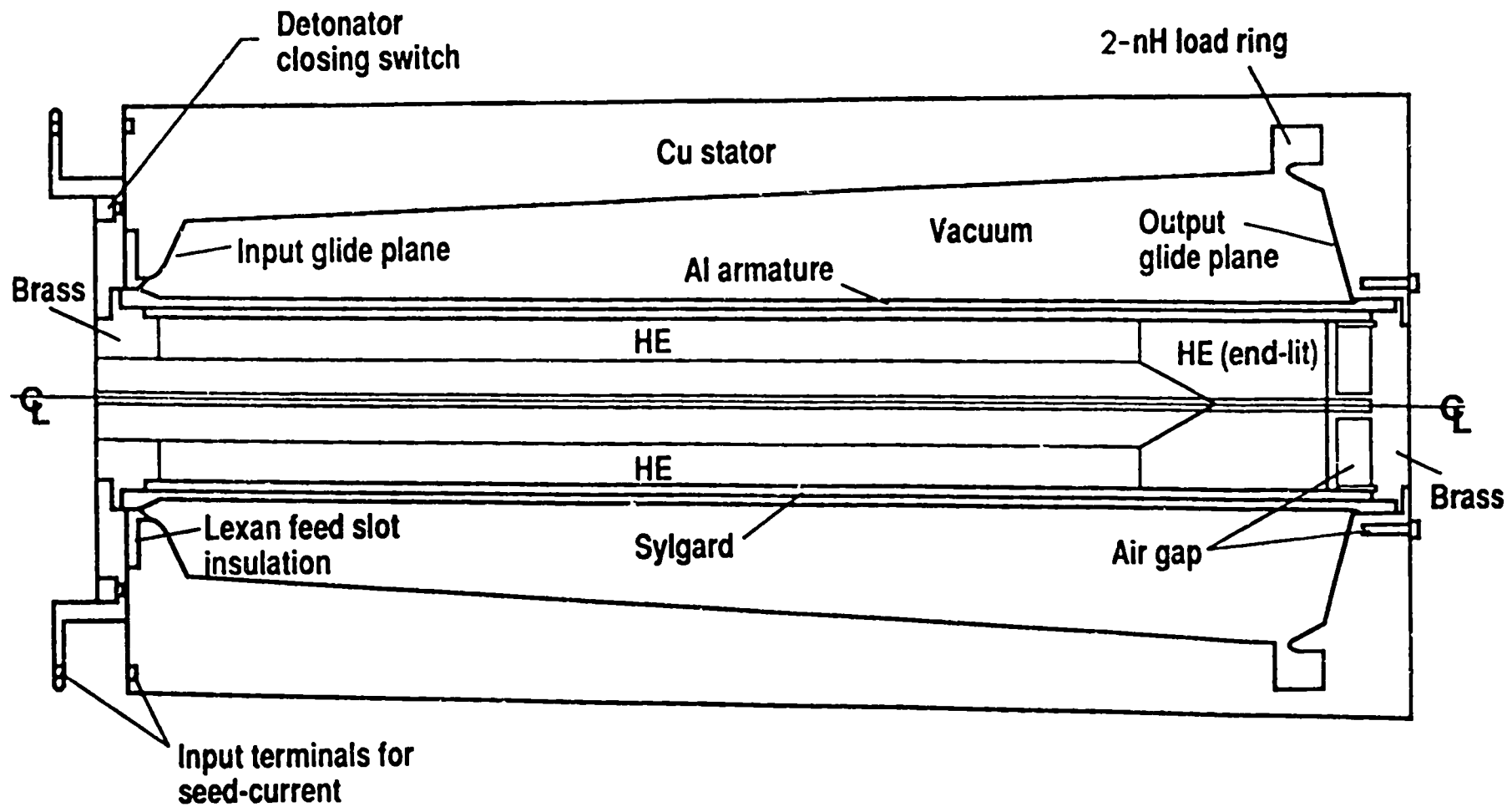
Fig. 1. CN-III simultaneous coaxial FCG as tested in the low- and medium-current experiments.

generator burnout as a way of controlling resistive losses during the high-current phase of flux compression. This was thought to be crucial to high efficiency since resistive losses scale as

$$E_R = \int_0^t d\tau \int_0^{l(\tau)} ds \int \int_{\sigma(s,\tau)} dA[\eta j^2] = \int_0^t d\tau R I^2$$

where the integrations are over time, current path length, and cross-sectional areas defined by the current skin depth, $\sigma(s,t)$. The symbols η and j are the generator resistivity around the current path and the current density, respectively. The symbols R and I are the time-dependent effective generator resistance and the total generator current. From this equation, there are two obvious ways to reduce resistive losses in an FCG. One way is to reduce the current path length during the high-current phase of flux compression by introducing a propagating section. The other way is to shorten the time interval during which the current is high. Not surprisingly, these two ideas are at odds. Introducing the propagating section to shorten the current path length near burnout, lengthens the generator run time.

Another consideration when trying to optimize generator output and maximize the efficiency of conversion of HE energy to magnetic-field energy, is that a significant length of the armature must work against a magnetic field that is strong enough to impede its motion to extract significant kinetic energy from a moving armature. However, strong magnetic fields compressed by significant lengths of moving armature necessitate high-current densities over long-current paths. This implies that more kinetic energy could be converted into magnetic-field energy at the expense of dissipating more field energy through resistive heating of the armature. However, since hotter armatures have higher resistivities, and strong magnetic fields have associated pressures that can easily exceed the driving pressures produced by HE, there exists a nonlinear feedback mechanism that limits FCG performance at some point. Therefore, minimizing resistive losses, as suggested by the above equation, is not the whole story.

A 1.27-cm layer of Sylgard is located between the HE and the armature. The primary purpose of the Sylgard layer is to smooth the shock front that drives the armature and thereby assure armature integrity throughout its expansion. Sources of nonsmooth driving conditions are varied, but include glue joints between Falcon modules, grain structure associated with the pressed explosive, imperfections in the HE surface, and residual structure produced by the initiation system. Several materials were tested in a series of planar experiments to define the best smoothing layer. Some of the materials tried were air, low-density polyurethane, low-density polystyrene, Sylgard, glass beads in Sylgard, and nothing (i.e., putting the HE directly in contact with the armature). As a result of these experiments, a 1.27-cm-thick Sylgard layer was chosen for the CN-III. The importance of assuring that this layer was homogeneous and contained no air pockets or gaps led to special precautions and assembly

procedures. A discontinuity in the Sylgard layer would have seeded an armature instability with serious consequences. A search for a material, or combination of materials that will both smooth the detonation front and mitigate the shock without dissipating too much of its energy, is continuing.

The input and output glide planes, like the stator, were also machined out of single pieces of spun-cast copper. The input and output glide planes were canted toward the center of the generator to insure good dynamic electrical contact as the armature expanded. The glide-plane angles and placement relative to the ends of the Falcon modules were designed with 2D hydrodynamics calculations. Following the case-motion test, the angles and relative placements were redesigned to minimize the observed "jetting" at the contact points and a lip was added to the output end to protect diagnostics in the load ring. The angles chosen for the low- and medium-current experiments were 15° and 23° for the input and output glide planes, respectively. Both angles were increased to these values from 5° used in the case-motion test based upon analysis of the test data and refined postshot calculations.

The load ring was a 2-nH fixed-inductance ring machined into the output glide plane with a 2-cm opening at the maximum radius of the stator. It was specifically designed with a low surface-to-volume ratio to minimize resistive skin losses and to minimize the inductance change associated with load-ring wall motion induced by the high-magnetic field. The load ring was placed on the outer radius of the CN-III to protect it and the diagnostics it contained from HE damage prior to FCG burnout. Strategically placed air gaps next to the explosive charge and in the glide-plane wall also helped to protect the load ring from HE-driven shocks.

The CN-III was assembled with only three high-current joints. These joints were made electrically sound through the use of indium o-rings. A vacuum of 10^{-5} torr was maintained in the inductive volume of the CN-III to prevent premature breakdown across the load-ring gap.

The input feed slot was insulated with a lexan ring and 0.127 cm of layered polyethelene sheets. Coaxial cables were used to supply the seed-current to the CN-III, and a ring of HE detonators served as a closing switch to short the input feed before first armature motion by driving jets through the layers of polyethylene film. This trapped the seed field in the working volume of the generator and isolated it from the initial current source.

The initial CN-III inductance for the low- and medium-current experiments was 203 nH plus the 2-nH load ring. Ideal current gain for these two experiments is therefore 102.5:1, assuming that all of the generator inductance is wiped out at burnout. This is a good assumption for the low-current test, but not necessarily valid for the medium- and high-current experiments. Armature velocities for the low- and medium-current tests, as measured in the case-motion experiment, were 0.22 cm/μs, which gives a total operating time of 87 μs

from armature first motion to generator burnout. The end-initiated solid Falcon added 20 μs to the final stage of flux compression relative to the computed operating time for an all-simultaneous CN-III of the same dimensions.

IV. CASE-MOTION EXPERIMENT

A. Purpose

The purpose of the case-motion experiment was to observe and measure the hydrodynamic motion of the armature in the absence of magnetic fields and to benchmark the hydrodynamics of the 1D and 2D MHD codes that were to be used for predicting the three subsequent experiments. The following specific objectives motivated the need for the case-motion experiment. They were

1. verify armature integrity and smoothness throughout its expansion,
2. examine the armature/glide-plane dynamic contact,
3. check that the glue joint between two simultaneous Falcons does not transmit a disturbance to the outer diameter of the expanding armature,
4. check that the transition between the simultaneous and propagating detonation regions does not cause serious perturbations,
5. check that all perturbations from the HE initiation system have been smoothed,
6. measure the armature expansion velocity, and
7. investigate the effects of irregularities in the armature surface.

B. Experimental Description

The case-motion experiment for the CN-III used a 1/2-length armature section that was driven by two Falcon modules and a solid Falcon. Glide planes, made of brass rather than copper, were attached to both ends of the armature. The glide planes were tilted toward the center by 5° as in the original CN-III design. The stator was not included as part of the experiment so that side-on framing-camera pictures of the expanding armature would be unobstructed. The entire assembly was enclosed in a Plexiglas box and flooded with helium to eliminate the background glow that would have come from shocked air at first armature motion. Two mirrors were placed in the helium box and turned to provide a view of the armature/glide-plane contact, which would have otherwise been obscured by the glide plane itself. Several scratches and one gouge (about 1-mm × 2-mm wide and 0.5-mm deep), which were collected on the armature during manufacture, assembly, and shipping, were noted and marked to evaluate their effect on instability growth. During the armature expansion, 70-mm color framing-camera pictures were taken at the rate of one picture every 3.3 μs and compared to preshot calculations.

C. Preshot Calculations

The first calculations were done on the fully implicit, 1D Lagrangian MHD code RAVEN.[1] RAVEN has an external circuit that provides boundary conditions for calculations of 1D, multimaterial meshes in planar, cylindrical, or spherical geometry. Realistic tabular equations of state (EOS) and electrical resistivities are obtained from the SESAME Library. RAVEN also contains a simple ideal gas-like HE EOS and a programmed-lighting-time model for detonation.

One-dimensional cylindrical calculations of the expanding armature, in the absence of magnetic fields, were done on RAVEN. Figure 2 shows interfaces as a function of time for a cylindrical section as predicted by RAVEN. Actually, this calculation includes the fields associated with the low-current experiment, but the fields, because they are small, have no noticeable effect on interface positions. The RAVEN calculation used the SESAME EOS 3715 for the aluminum. The predicted armature velocity is shown in Fig. 3, with the velocity averaging ~0.28 cm/μs. Multiple RAVEN calculations varying zoning resolution and EOS's were performed. Figures 2 and 3 serve as representative samples of these calculations. Figure 4 shows a pressure profile through the armature just prior to shock breakout. Shock strength determines armature temperature and hence its electrical resistivity. It also controls the severity of "fluff" generation and has an effect on spall. Achieving a gentler but prolonged push on the armature has motivated the search for a good shock-mitigation layer between the HE and the armature.

Fig. 2. Predicted interface positions for CN-III driven by the simultaneous Falcon modules for both the case-motion and low-current experiments. Calculations are from RAVEN using the default HE parameters for PBX-9501.
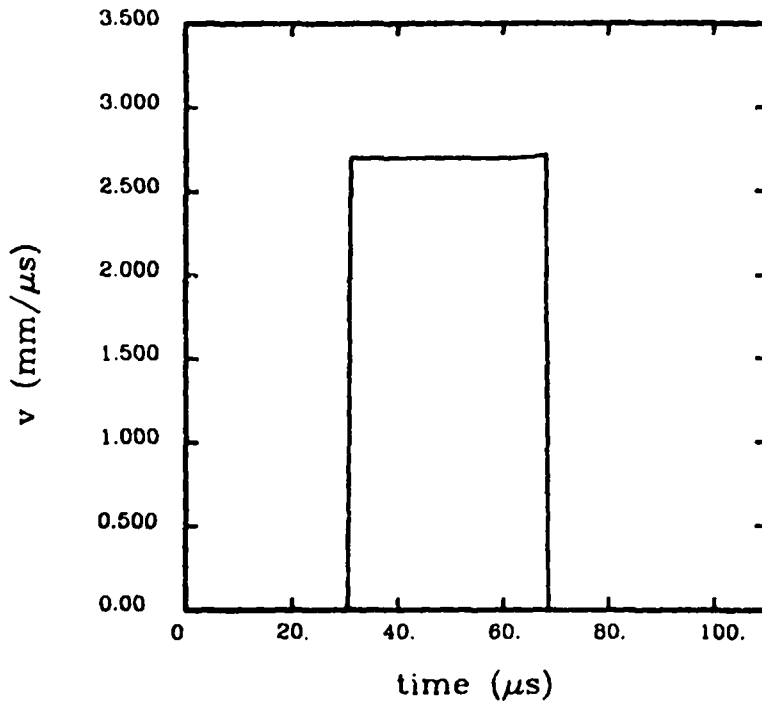
Fig. 3. Predicted armature velocity for CN-III driven by the simultaneous Falcon modules for the both the case-motion and low-current experiments. Calculations are from RAVEN using the default HE parameters for PBX-9501.
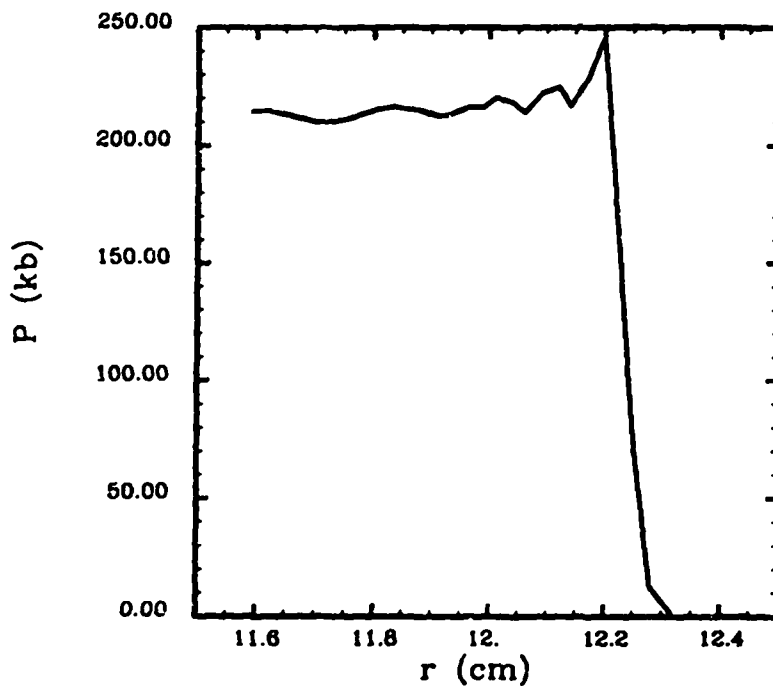

Fig. 4. Predicted pressure profile for CN-III armature driven by the simultaneous Falcon modules for the case-motion experiment. Calculations are from RAVEN using the default HE parameters for PBX-9501.

One- and two-dimensional calculations for the case-motion experiment were performed on a 2D, explicit-hydro Eulerian MHD code that uses an implicit algorithm for the solution of the MHD equations. Calculations for the CN-III experiments were done using an energy-based scheme and analytic EOS models. No MHD options were exercised in the Eulerian code for these calculations. Comparison of the 1D calculations with the RAVEN results established an appropriate level of zoning resolution that could be used in the subsequent 2D calculations. The HE model in the 2D code uses a programmed-lighting time with a JWL EOS. Two significant differences between the predictions of the 2D code and RAVEN were that the armature shock structure is not as well resolved by the 2D Eulerian code and that the armature velocity predicted by the 2D code is 0.23 cm/μs. Since the HE package in the 2D code had been benchmarked against previous case-motion experiments in similar geometries, the RAVEN result was considered anomalously high and was attributed to the overly simple HE model. The velocity was crosschecked with calculations on another hydro-only Eulerian code used in M-6 for EOS studies. These calculations provided further confirmation that the armature expansion velocity should be close to the predicted 0.23 cm/μs.

Full 2D calculations of the case-motion experiment, including the simultaneous-to-propagating transition and the output glide plane, are shown in Fig. 5. Zoning resolution in the calculation is 0.5-mm radial by 5.0-mm axial. Hints of a jet or spray of material at the armature/glide-plane contact are just visible, and good contact seems to be maintained throughout the expansion. The armature shape across the Falcon/solid Falcon interface is distinct and indicates the possibility of an armature integrity problem. The questions raised by these preshot calculations emphasize the importance of performing the case-motion experiment and its value relative to benchmarking of the 1D and 2D codes.

D. Comparison of Calculations and Experiment

Data from the case-motion experiment were in the form of excellent quality color photographs. From measurements taken off of the pictures, the armature velocity was determined to be 0.22 ± 0.02 cm/μs, with no significant difference between the simultaneous and propagating sections. Armature integrity throughout the expansion was verified, with the transition between the Falcon and solid Falcon shaped as predicted and indicating no signs of weakness. During the expansion, the section of the armature driven by the simultaneous Falcons showed ~0.1 cm "stretch marks" with a transition to a smooth surface for the propagating section. When viewed from end-on, the stretch marks formed a fluted pattern around the armature. No indication of perturbations from the initiation system were evident. However, HE or decomposed Sylgard gases did vent through the deep gouge in the armature. The small scratches that were accumulated during shipping and assembly seemed to cause no major problems, but procedures to avoid them were implemented in subsequent shots.
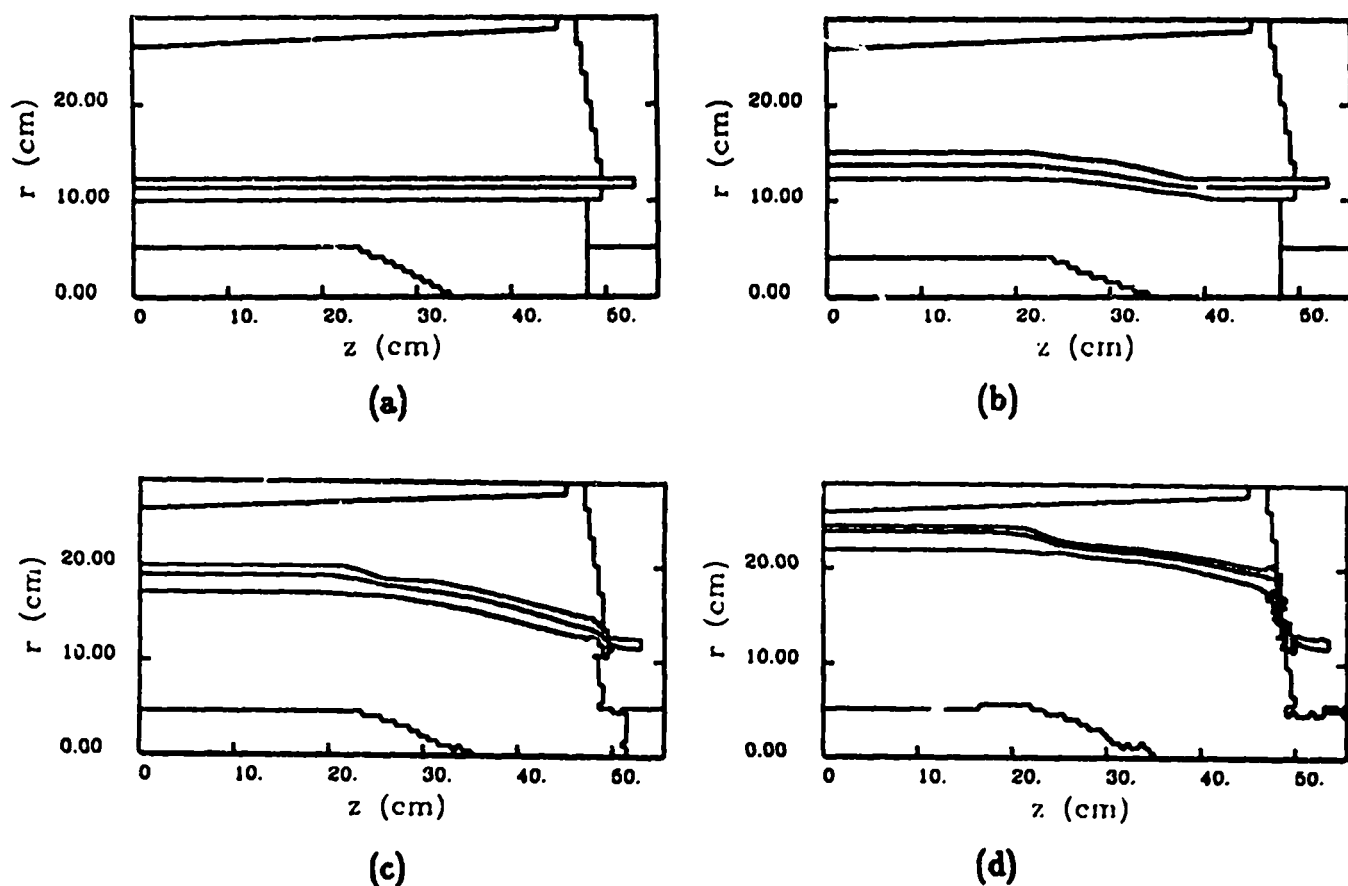
12

Fig. 5. Preshot 2D calculations of the case-motion experiment showing the output end and the Falcon/end-lit transition. Coarse axial zoning is evident from the stair-stepped interfaces. Snapshots a–d are shown at 0, 20, 40, and 60 μs, respectively.

The hints from the preshot 2D calculations that jetting at the armature/glide-plane interface might be a problem proved to be well founded. The input glide plane showed a severe "splash" as the armature closed off the input feed slot by making contact with the glide-plane wall. This was followed by a continued jetting of aluminum and/or brass (glide-plane material) from the contact point as the armature expanded. The output glide-plane contact showed the same jetting, but more seriously, the pictures showed the presence of HE or decomposed Sylgard gases mixed with the metal "spray." The breakthrough of gases around the armature signaled the possibility of a circuit disconnect, or at best, a high-resistance path, during flux compression. The other disconcerting aspect of the output glide-plane jet was that it would have impinged directly on the load-ring opening, raising the probability of premature shorting of the gap and/or destruction of load-ring diagnostics.

E. Calculational Redesign

The redesign of the glide planes and the load ring proceeded in two steps. First, the 2D code was used with much finer resolution to calculationally reproduce the data collected from the case-motion experiment. Sensitivity studies with variations on EOS's, strength models,

13

artificial viscosity parameters, and zoning resolution were conduc· ·   ι the conclusion that zoning is by far the most important variable. To get acceptable agieement with the data on the input and output glide-plane jets, the axial zoning resolution in the 2D Eulerian code had to be improved to 0.25 mm in the area around the glide planes. Material strength makes almost no difference in the calculations since the initial shock from the HE and the rarefaction following shock breakout at the armature surface heat the aluminum almost to the melting temperature and cause a reduction in density below the reference density. The outer surface of the armature expands slightly faster than the inner diameter causing a reduced density. Both of these factors tend to diminish the effect of material strength. The actual manifestation of this code prediction may be "virtual" spall of the armature around the simultaneous Falcon sections. The density reduction in the armature was not seen for the propagating section. The improved input and output glide-plane calculations are shown in Figs. 6 and 7. The perturbation in the armature between z = 36 cm and z = 40 cm, which appears in the output-end calculation of Fig. 7, is an artifact of the closed-boundary condition.

The second step of the glide-plane and load-ring redesign was accomplished with multiple, fine-zoned, 2D calculations to reduce the severity of the jets and eliminate blow-by at the output end. Design modifications that were explored involved varying the convergence angle of the glide planes, moving the glide plane relative to the end of the explosive charge, inserting air gaps and cutters, plus moving the opening of the load ring to protect it from any spray that does occur. Changes were restricted by the fact that the stators for the next three experiments and all six glide planes had already been cast. Input and output glide planes could be remachined. However, the stators were too big and heavy and expensive to modify. Five specific conclusions were reached in the redesign study:

1. Cutter technology and any design that favors a sliding contact causes problems in this application. If the armature slides along the glide plane, HE gases are likely to vent past the contact point, leading to a high-resistance current path. Large convergence angles coupled with sliding contacts cause a buildup of mass in front of the sliding contact. This excess mass is launched ahead of the armature forming a jet.

2. Small convergence angles coupled with a glide plane, which starts close to or inside of the axial extent of the HE charge, have the tendency to "tent peg" the glide plane, causing the armature to separate from the glide plane. Tent pegging describes the motion of the glide plane when its inner diameter is shocked by the expanding armature. The glide plane spreads axially like a wooden tent peg being driven with an axe. The trailing ends of the armature that have separated from the glide plane, except at the point of tent pegging, thin and break, or more likely, fuse under the influence of large currents.

14

3. Moving the glide planes too far outside of the axial extent of the HE charge causes too much thinning and a stretching of the armature before contact is made with the glide plane.

4. The spray can be minimized by moving the glide plane as far as possible outside of the HE, keeping armature thinning in mind, and using large enough convergence angles to encourage the armature mass, which builds up at the point of contact, to be left behind instead of thrown ahead. The ideal armature/glide-plane interaction involves laying the armature against the glide plane rather than sliding past it.

5. Finally, the spray cannot be completely eliminated under the constraint that good electrical contact must be maintained.

Calculations of the redesigned contacts are shown in Figs. 8 and 9. The input and output glide-plane angles have been increased to 23° and 15°, respectively, and the output glide plane has been moved further outboard relative to the HE termination. The output end also has incorporated strategically placed air gaps to diffuse shocks and protect the load ring. The load-ring opening has also been moved to protect it from the unavoidable spray.

V. LOW-CURRENT CN-III
A. Purpose

The purpose of the low-current CN-III experiment was to characterize the generator in the traditional FCG operating regime. At LANL, most FCGs have been operated under low-current-density conditions such that a high efficiency of conversion from chemical energy to electromagnetic energy has not been required. Magnetic fields within a typical generator never get high enough, early enough in the run, to cause a significant slowing of the armature. Flux conservation efficiencies under these conditions range from $\leq 30\%$ for large high-gain spiral generators to $\geq 70\%$ for end-initiated coaxial generators. This first "live" test of the CN-III verified that the generator would perform as expected in the low-current-density regime and confirmed that the purely calculational redesign of the glide planes was adequate. The test also provided a valuable benchmark for the MHD codes, EOS's, and electrical resistivity models that were used in modeling subsequent CN-III experiments.

B. Computer Modeling with RAVEN

Preshot calculations of the CN-III were done on RAVEN, running in a quasi-2D mode. The main driver for RAVEN is a sophisticated, multiloop, electrical circuit package that allows time-dependent inductances, resistances, and capacitances. It also allows "zero-dimensional" circuit elements, which can be tailor-made to model anything from fuses and plasma compression opening switches to FCGs and z-pinch implosions. The main purpose of the circuit package driver is to provide realistic, time-dependent boundary conditions for the MHD equations in the 1D module that, in turn, feed back self-consistently to the rest
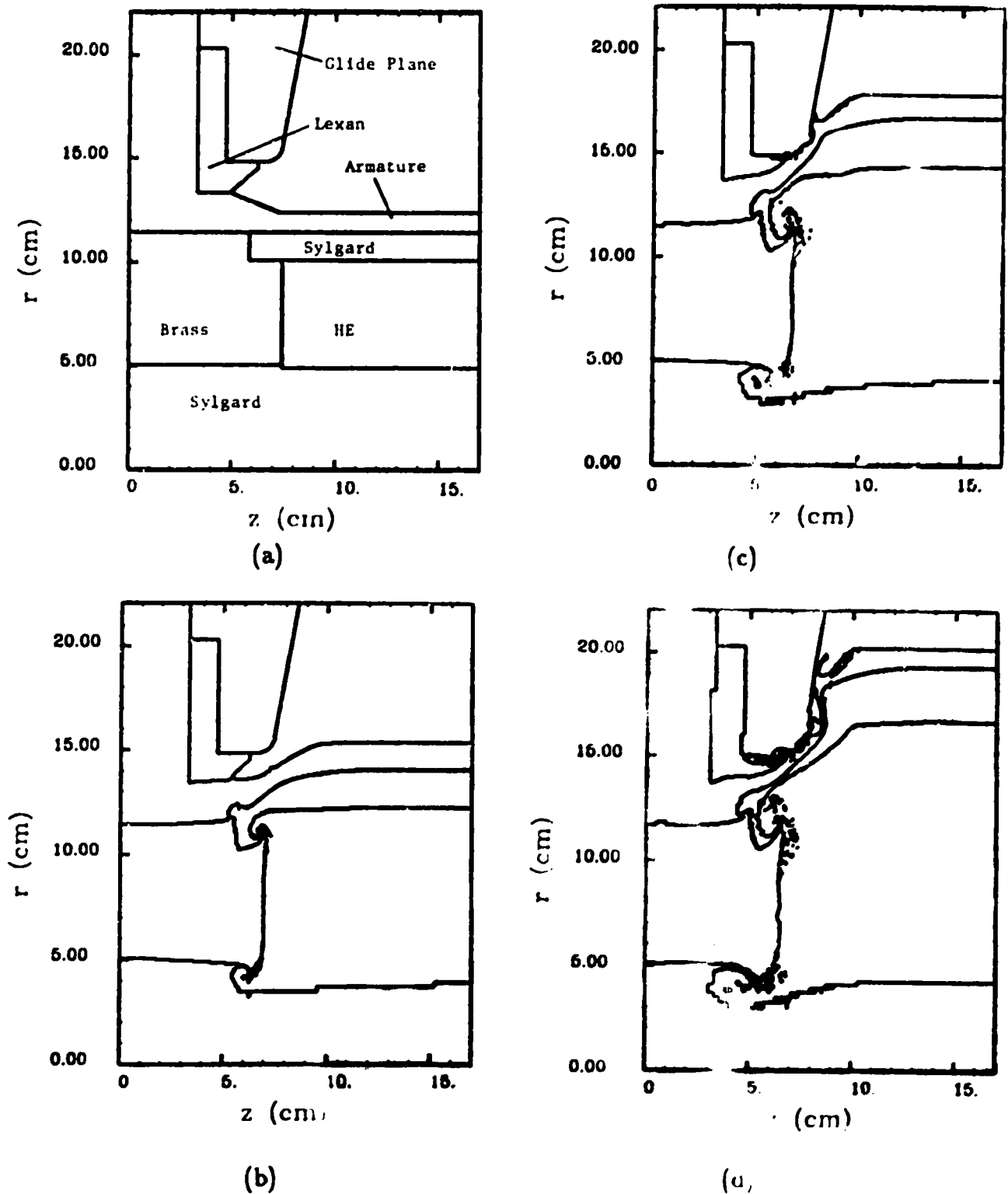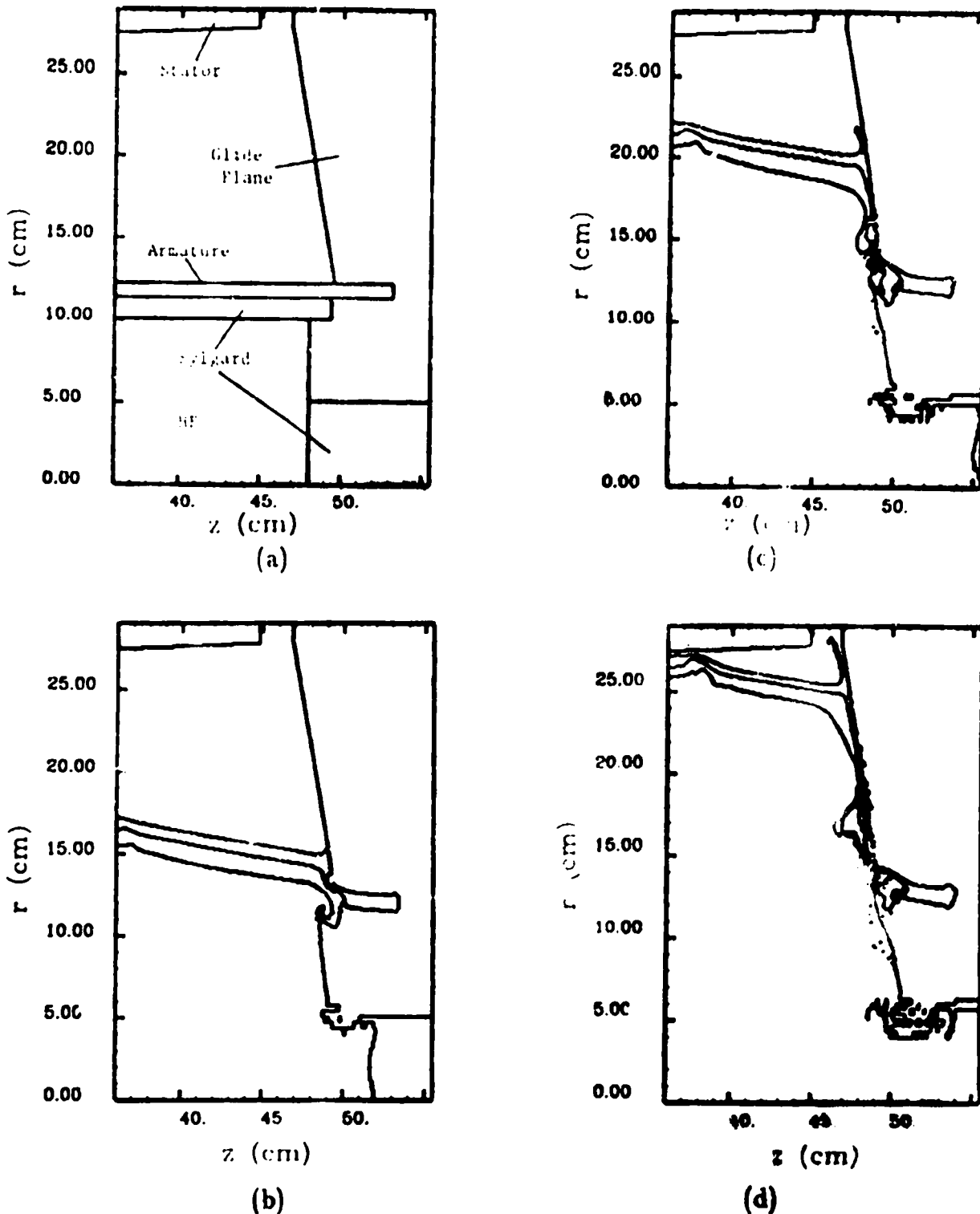
15

Fig. 6. Case-motion fine-zoned 2D postshot calculations of the input end showing "jet" formation. Times for a–d are 0, 20, 30, and 40 μs.
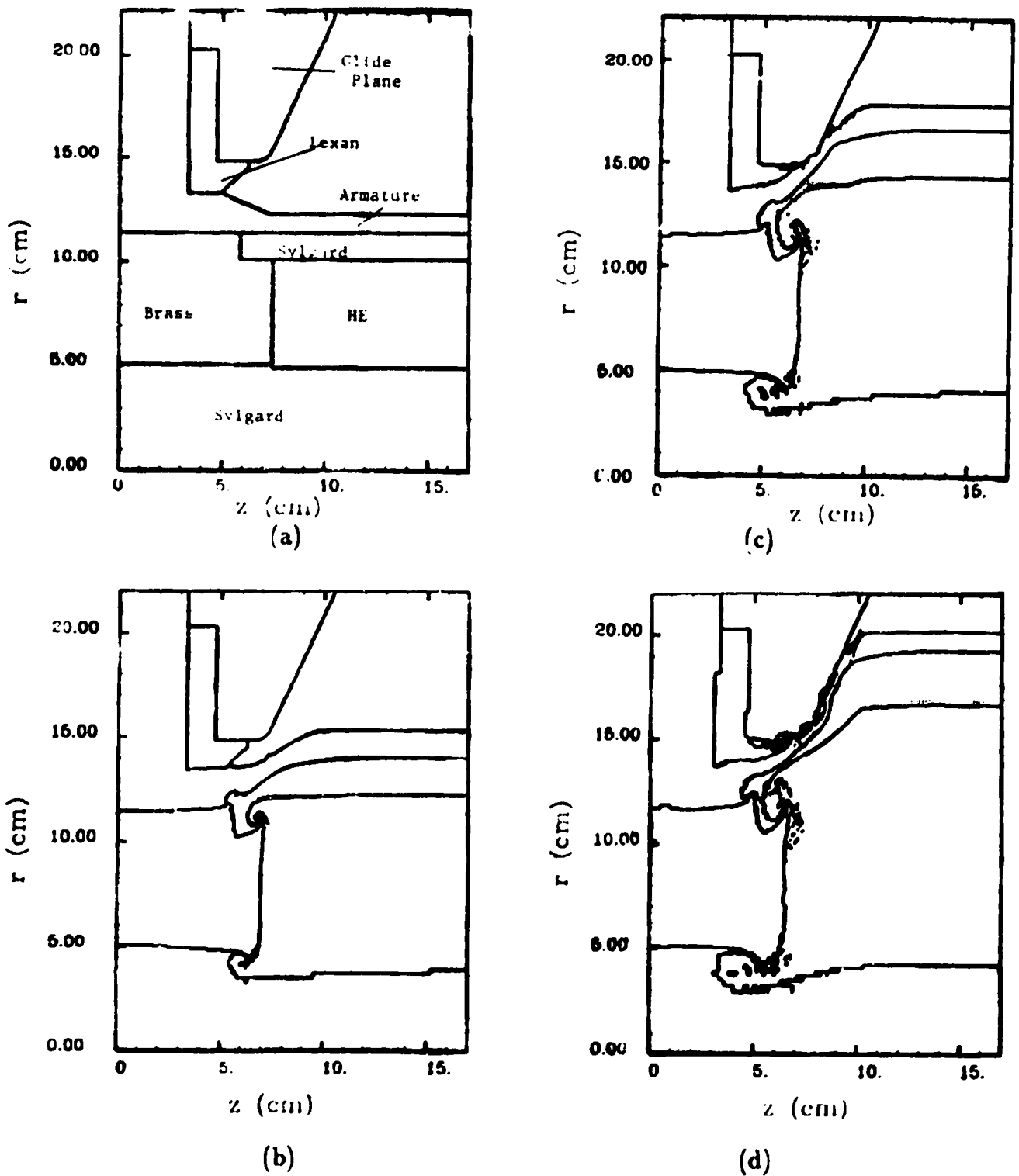
of the circuit. The circuit package is flexible enough that multiple 1D MHD modules can be run simultaneously and be self-consistently coupled through their interaction with the circuit. Each module can be divided into similar submodules that are also coupled through the circuit.

This allows RAVEN to be run in a vectorized mode over submodules. Different modules can be very different without incurring undue calculational penalties since the vectorization takes place over similar submodules.

Fig. 7. Case-motion fine-zoned 2D postshot calculations of the output and showing "jet" formation. Times for a-d are 0, 30, 50, and 70 μs.

Fig. 8. Fine-zoned 2D calculations of the redesigned input end. Times for a-d are 0, 20. 30, and 40 µs.

The capability of running multiple, simultaneously coupled, 1D MHD simulations in RAVEN allowed the modeling of the principal 2D character of the CN-III without the difficulties, complexity, and expense associated with a full 2D MHD simulation. The CN-III is 1D

18

in the sense that hydrodynamic motion is almost entirely in the radial direction, even in the region of the solid Falcon. The main shear flow occurs at the input and output glide planes. The 2D nature of the CN-III is a result of the built-in phasing angle of the stator, and the

(a)

(c)

(b)

(d)

Fig. 9. Fine-zoned 2D calculations of the redesigned output end showing reduced "jet" formation and protected load ring. Times for a–d are 0, 30, 50, and 70 μs.

axially propagating detonation wave in the solid Falcon that delays first armature motion near the output end relative to the jump-off time in the region of the simultaneous Falcons. Adjacent axial sections of the CN-III communicate with each other through the trapped magnetic field, which transmits signals at light speed. Dividing the CN-III into 10 sections with imaginary planes, perpendicular to the axis, and then approximating each section as a 1D RAVEN MHD module or submodule proved to be a realistic and reasonable approach to accomplishing quasi-2D simulations. The module representing the input end was 25-cm long, whereas the output end module was only 4 cm. Intermediate modules varied smoothly in length between these extremes. Each module had a different stator radius to model the phasing angle, and the last four modules in the region of the solid Falcon had delayed detonation times to model the sweeping detonation wave. A schematic illustration of the multimodule RAVEN simulations for the CN-III is given in Fig. 10. RAVEN automatically terminates the calculation of a module or submodule upon armature/stator contact and removes it from the circuit.

RAVEN Simultaneous Multimodule MHD

Fig. 10. Schematic diagram of RAVEN multimodule MHD calculations for the CN-III.

For the low-current experiment, the RAVEN calculations modeled one module of the Firing Point 88 capacitor bank with a 1.5-mF capacitance charged to 14 kV. Appropriate resistances and inductances were included in the circuit to properly model the internal bank parameters and the feeder cables from the bank to the CN-III. The HE-driven, crowbar switch, which has been on the CN-III, was modeled by a fast time-varying resistance. This extends the circuit a 1.0-MA seed-current to the generator. Variations in electrical resistivity models and EOS's produced predicted peak currents in the range of 60 to 80 MA. To verify that the propagating portion of the armature reduces skin losses by shortening the current path length during the high-current phase of flux compression, two calculations using identical zoning, EOS's, and electrical resistivities, one with a propagating section and one completely simultaneous, were compared. The simulation, which included the propagating section, showed a peak current of 10 MA larger than the all-simultaneous calculation.

The preshot-calculated current profile for the low-current experiment is given in Fig. 11. The peak current from Fig. 11 is 71 MA, with an expected uncertainty that was reported preshot as ±10 MA. The simple HE model in RAVEN pushes the armature slightly faster than was measured in the case-motion experiment. Therefore, the operating time predicted by RAVEN was expected to be ~10% shorter than measured. The calculated peak voltage across the load-ring gap of 9 kV was also expected to be high because of the "too-high" armature velocity. These preshot predictions were made using SESAME EOS 3715 for the aluminum and a modified More resistivity table.[9-11] Uncertainties in the calculations other than those associated with the HE model, the EOS's, the resistivity model, and the difficulties of modeling a 3D process with a quasi-2D code, include the coarse axial resolution allowed by only 10 submodules and the inability to model flux losses at the glide planes in a consistent manner.

Fig. 11. Preshot calculated output current for the low-current CN-III experiment from multimodule RAVEN.

Plots of material interface radii and armature velocity versus time for the RAVEN calculation were shown earlier in Figs. 2 and 3 for the input end driven by the simultaneous sections. Similar plots for the output end are shown in Figs. 12 and 13. The effect of reflected signals from the discontinuities associated with layers of Sylgard and HE is seen as an acceleration of the armature beginning at ~60 μs. Figure 13 also illustrates the effects of the magnetic back-pressure as the current increases. The slight slowing down of the armature near the end of the trace is indicative of the conversion of HE energy into electrical energy.
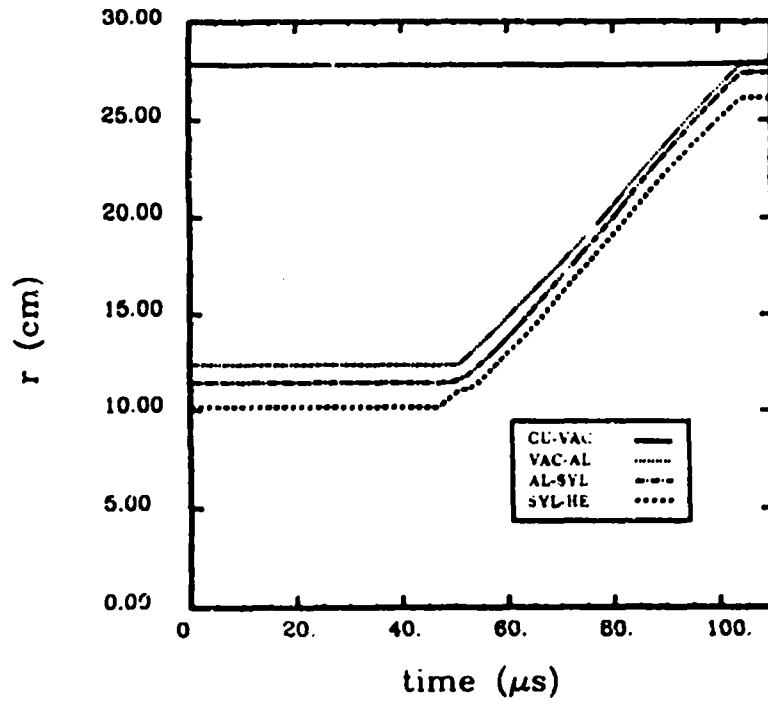
21

Fig. 12. Predicted interface positions for the output end of the CN-III driven by the end-lit Falcon module for the low-current experiment. Calculations are from RAVEN using the default HE parameters for PBX-9501.
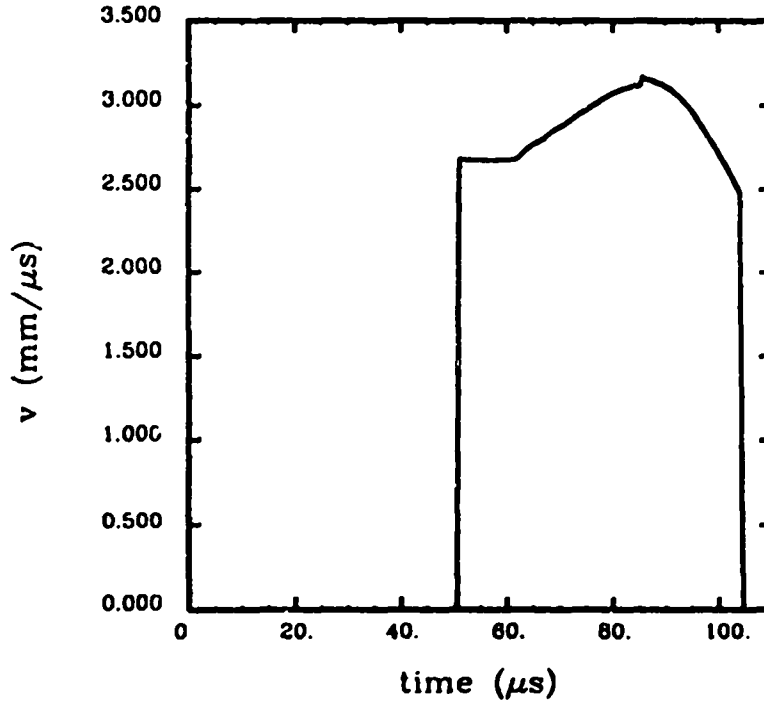

Fig. 13. Predicted armature velocity for the output end of the CN-III driven by the end-lit Falcon module for the low-current experiment. Calculations are from RAVEN using the default HE parameters for PBX-9501.

C. Experimental Results

The initial seed-current for the low-current CN-III experiment, provided by one module of the Firing Point 88 capacitor bank charged to 14.1 kV, was 0.98 ± 0.05 MA. The final output current of 68 ± 4 MA was measured by a Rogowski loop located in the load ring. The current derivative signal from the Rogowski loop is presented in Fig. 14. The integrated signal, giving FCG current, is displayed in Fig. 15 and indicates a peak current of 68 MA with an estimated uncertainty of ±4 MA. At this time, all inductance in the main FCG volume has been eliminated and the controlled experiment is over. The current derivative jumps again as the load ring is compressed, sending the integrated current well above 70 MA. Flux conservation efficiency for the CN-III in this low-current-density regime is a very respectable 68%. Other diagnostics included four dB/dt loops and two Faraday rotation fibers in the load ring, two Rogowski loops at the input, four capacitively coupled dV/dt probes in the load-ring opening, an electro-optical crystal for measuring load-ring voltage, and hydrodynamic probes. The peak inductive voltage across the load-ring opening was measured to be 8 ± 1 kV. This value is consistent with the result obtained by multiplying the load inductance, 2 nH, by the current derivative. The Faraday rotation probes track well with the Rogowski loops until the point at which the Faraday fibers were damaged by wall motion of the generator. The hydrodynamic probes, which consisted of various lengths of optical fiber threaded along the output glide plane and the stator, returned no useable data.
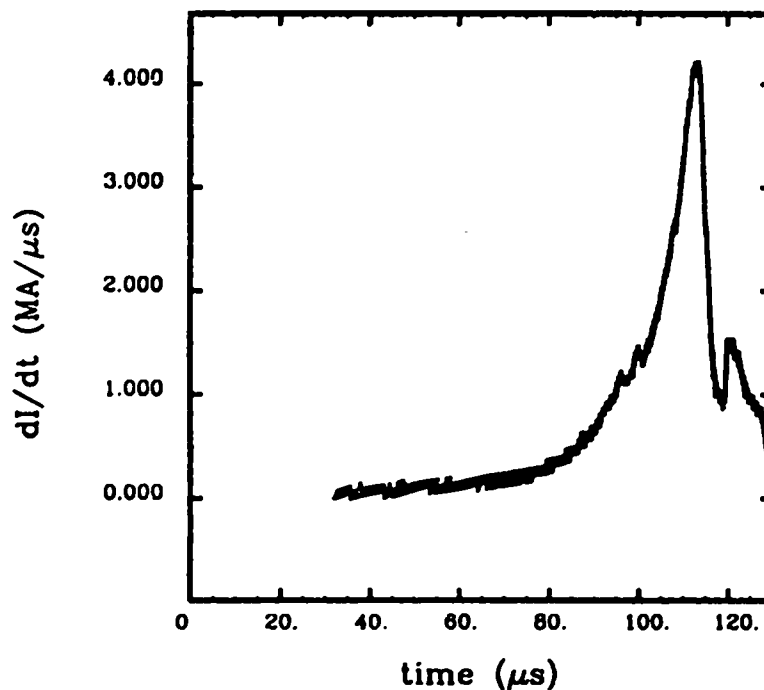

Fig. 14. Measured current derivative from the output-load-ring Rogowski probe for the low-current CN-III experiment. The discontinuity at 120 μs marks generator burnout. The trace for times after 120 μs indicates further flux compression by closing the load ring itself.
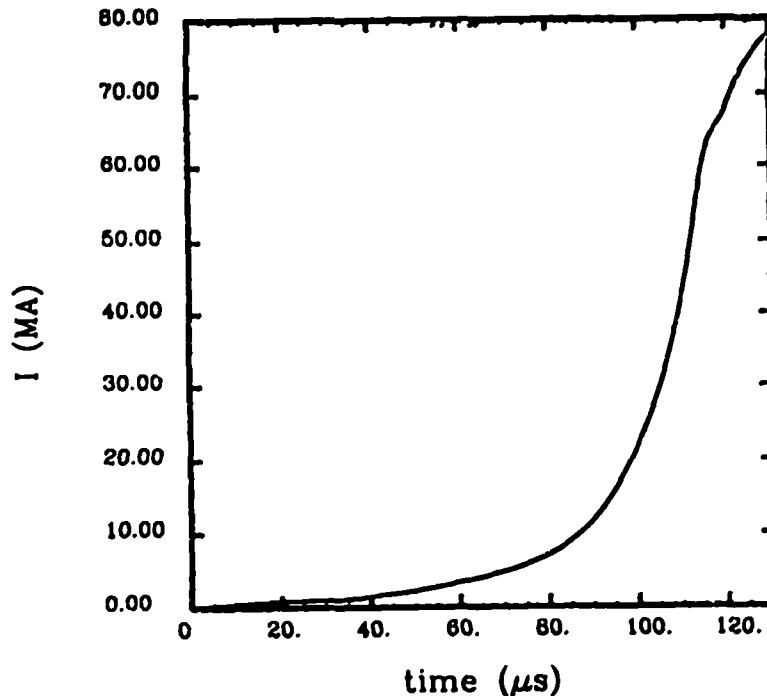
Fig. 15. Integrated-load-ring Rogowski probe signal. Peak current at generator burn out (120 μs) is 68 ± 4 MA. The signal beyond 120 μs is a measure of flux compression within the load ring.

In summary, quasi-2D RAVEN MHD calculations agree well with the low-current data, except for the timing discrepancy explained by the HE treatment. Use of RAVEN's multimodule capability was crucial for providing realistic simulations of the low-current experiment. Redesign of the glide planes was successful, and the armature carried current throughout its expansion with no apparent anomalies. Finally, the calculations confirmed that introducing the propagating section decreases flux loss relative to an all-simultaneous FCG in the low-current-density regime.

VI. MEDIUM-CURRENT CN-III

A. Purpose

The medium-current CN-III experiment was designed to approach the 1-MA/cm "rule-of-thumb" limit for the linear current density, which can be carried by an HE-driven, moving conductor. To approach this limit, enough initial magnetic flux has to be loaded into the generator to be sure that significant slowing of a portion of the armature will occur near generator burnout. Confirming that the armature would remain intact at higher fields during the slowing process was also an important goal. Extension of the calculations, which were benchmarked in the low-current-density regime, to this more demanding parameter range was a necessary step on the way to accomplishing the overall-series goal of predicting and achieving 150 MA.

24

B RAVEN Preshot Calculations

Given a good benchmark with excellent agreement from the low-current test, calcula-
tor the medium-current test were conducted with RAVEN using the same model. It
was determined that an initial seed-current of 3 MA was possible by using all four modules
of the Firing Point 88 capacitor bank charged to 18 kV. At this higher loading current, the
CN-III would naively deliver >200 MA if it were capable of maintaining the same efficiency
measured in the low-current experiment. However, such a current would significantly exceed
1 MA/cm on the moving armature.

RAVEN simulations, using the same model and geometry as used for the low-current
test, with seed-currents between 2.5 and 7.2 MA, gave peak currents of 135 to 140 MA. The
current profile for the 3-MA seed-current is given in Fig. 16. The explanation for this limiting-
current behavior, independent of initial seed-current, is readily understood by examining
interface profiles and the armature expansion velocity for the output-end RAVEN module in
Figs. 17 and 18. As the current reaches its peak of ~138 MA in the calculation, the magnetic
field stops and turns the armature around. This leaves magnetic flux in the uncompressed
inductance of the generator. The larger the initial current, the more inductance that remains
in the CN-III at armature turnaround. The behavior of the CN-III at the input end is
essentially identical to the low-current shot, since the current does not get large until most of
the inductance is gone. The efficiency of conversion from HE-chemical energy into magnetic-
field energy continues to increase with initial seed-current because of the increasing effective
load inductance, but the final current is limited by the HE-driven inertia of the armature
relative to the magnetic back-pressure.

For a 3-MA initial seed-current, RAVEN predicted that some fraction of the armature
would be stopped before making contact with the stator. This fraction begins at about the
simultaneous/propagating transition and continues to the output end. Since the armature
velocity was still predicted to be too high, generator timing was again not expected to match
the RAVEN calculations. An unknown effect on the peak current was expected because of
the "too-high" armature velocity. However, the effect was assumed to be small because of
the good agreement with the low-current data. A preshot expectation for the peak current of
130 ± 30 MA was used to set recording sensitivities for the experiment. The large uncertainty
arose from the fact that both calculations and relevant experience in the higher-current-
density regime were based on extrapolations from the low-current experiment.

C. Experimental Results

All four modules of Firing Point 88, charged to 18+ kV, delivered 3.0 ± 0.2 MA to the
CN-III. The medium-current shot was equipped with the same cadre of diagnostics as fielded
on the previous experiment. The output current, which peaked at 105 ± 5 MA, is shown
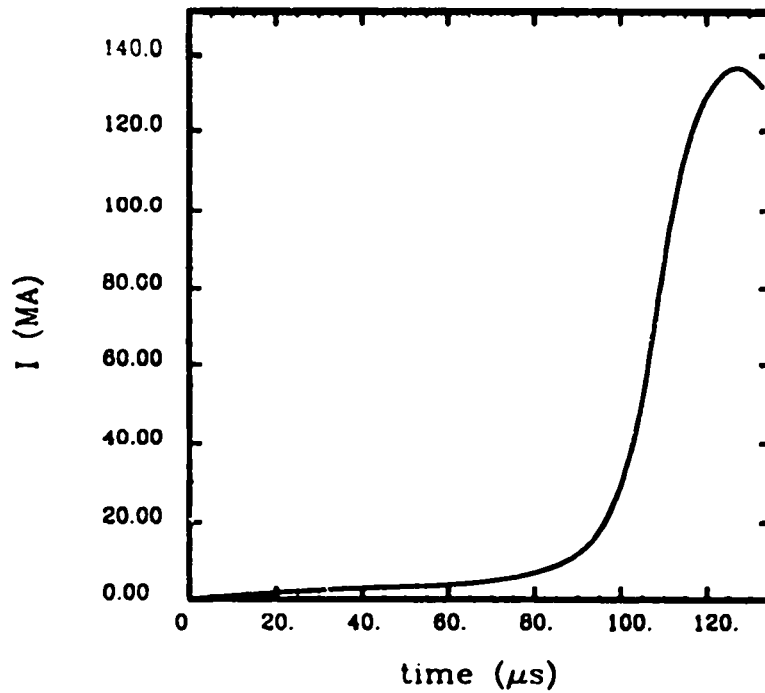
Fig. 16. Preshot calculated output current using 3.2-MA initial seed-current for the medium-current CN-III experiment. Calculations are done with multimodule RAVEN.
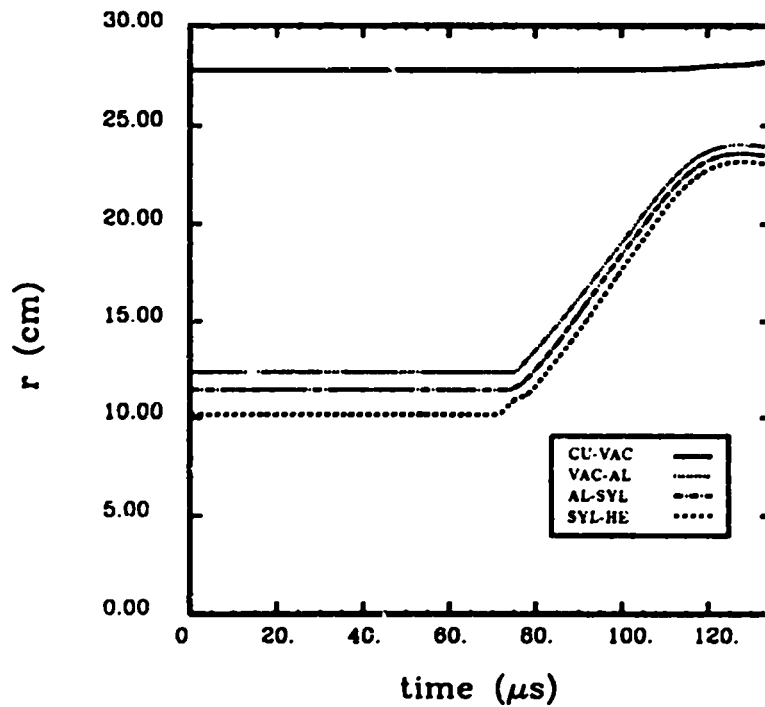

Fig. 17. Calculated interface profiles of the output-end RAVEN module using 3.2-MA initial seed-current for the medium-current CN-III experiment. Calculations are done with multimodule RAVEN.
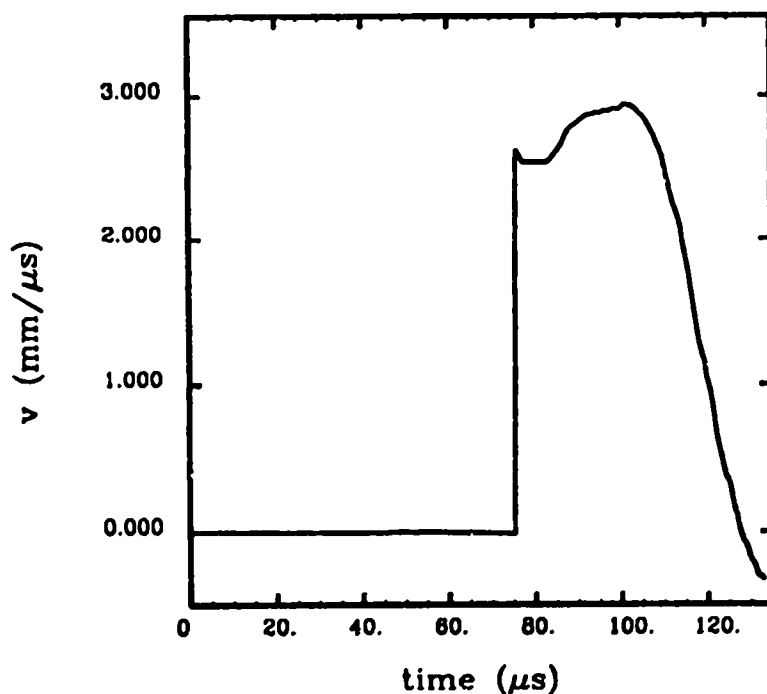
Fig. 18. Calculated armature velocity of the output-end RAVEN module using 3.2-MA initial seed-current for the medium-current CN-III experiment. Calculations are done with multimodule RAVEN.

in Fig. 19. The trace in Fig. 19 is integrated from the load-ring Rogowski probe measurement of dI/dt shown in Fig. 20. The Faraday rotation data followed the Rogowski data up to the point of premature failure of the optical fibers. Timing data and comparison with the low-current experiment indicated that the armature either stopped or broke up with about 2 to 4 nH left in the generator. An additional 2 nH in the fixed load implies an effective load inductance of 4 to 6 nH. Physical evidence in the form of large stator fragments with armature imprints and pieces of armature still attached, supports the conclusion that the armature did not collide with the stator over about the last 5 to 10 cm of stator length. Much of the sensitive data was not collected on this experiment because of a grounding problem within the bunker at Firing Point 88. Subsequently, part of the bunker's ground system was redesigned to protect against future compromises of the single-point grounding system.

D. RAVEN Postshot Calculations and Analysis

Leaps in understanding often come from analyzing experiments that yield unexpected results, and the medium-current CN-III experiment certainly provided this opportunity. The ±30 MA uncertainty cited above represented a conservative approach to the fear of the unknown. A more accurate accounting of our true expectations would have been a peak current of 130 to 135 MA. Therefore, a peak current of only 105 MA implied that something about our understanding of how to scale FCG operation to high-current densities was incomplete.
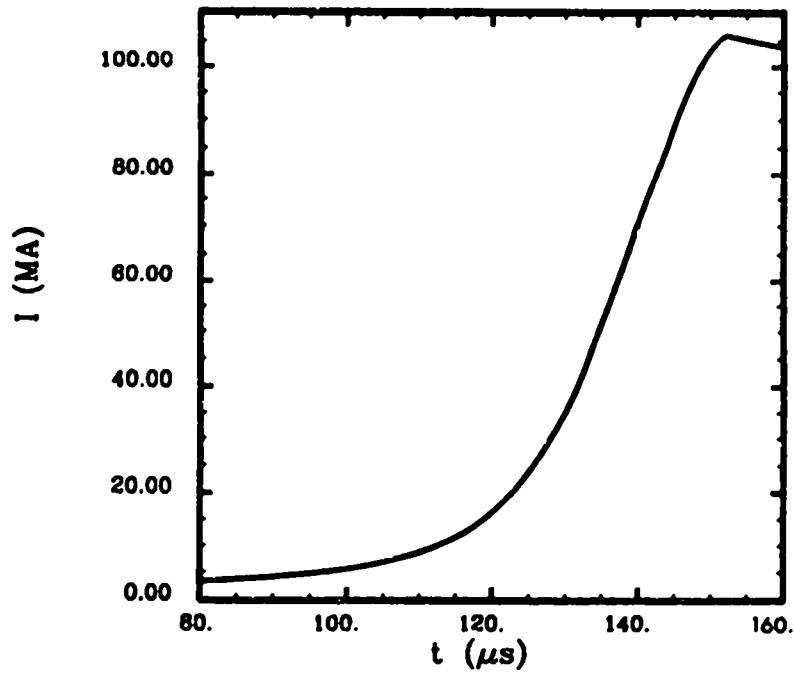
Fig. 19. Measured output current for the medium-current CN-III test. Current peak is 105 MA with an uncertainty ±5 MA.
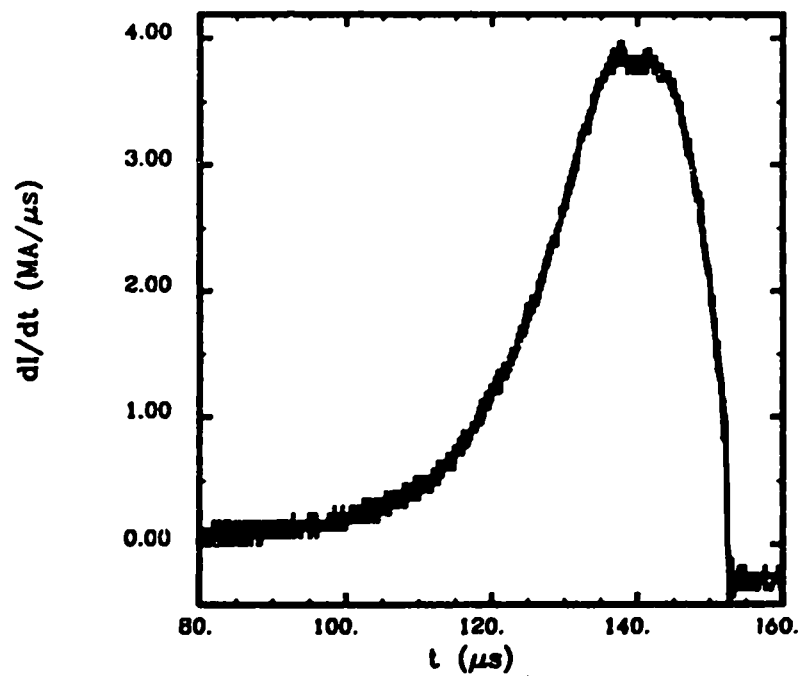

Fig. 20. Measured current derivative for the medium-current CN-III test.

Furthermore, without an improved understanding, achieving a 150-MA peak current in the last CN-III experiment would not have been possible.

An obvious shortcoming with the preshot calculations is the excess armature velocity predicted by RAVEN. The puzzle associated with the fact that the predicted peak current in the low-current experiment agreed well with the data, while the medium-current calculations were overly optimistic, is explained by the following argument. In the low-current experiment, most of the armature's kinetic energy was dissipated by collision with the stator. Only a very small fraction of the total kinetic energy actually is converted into field energy. Therefore, peak current is controlled almost entirely by the ratio of generator inductance to load inductance and flux losses in the generator. As long as the CN-III armature completely wipes out the generator inductance with excess kinetic energy, its peak current will be given approximately by

$$I_f = f_c\left(\frac{L_g + L_l}{L_l}\right)I_0 \quad ,$$

where the ratio of inductances (or the ideal gain) for the CN-III is 102.5 and the flux conservation coefficient, f_c, is 0.68. The equation should hold for initial currents, I_0, up to ~ 1.5 MA. In the simulation of the low-current experiment, the excess kinetic energy in the armature was manifest in the generator timing and the amount of energy wasted upon collision with the stator. The effect on current amplification was negligible. For the medium-current CN-III, a large fraction of the kinetic energy in the last section of the armature was converted into magnetic-field energy when the armature was stopped. In the preshot RAVEN simulation of the experiment, this section of armature contained excess energy because of its "too-high" velocity. This excess energy showed up as too much field energy and, therefore, a higher peak current than measured. By reducing the armature velocity in RAVEN to the value measured in the case-motion experiment, excellent agreement for generator timing and peak current were achieved for the medium-current experiment.

Two approaches were taken to bring the RAVEN-calculated-armature velocity into agreement with the case-motion data. The first was to scale the energy release of the ideal gas HE EOS low enough to sufficiently reduce the energy deposited in the armature. The HE EOS in RAVEN has the form

$$P = c_2\, T\left(1 - \frac{1}{c_5\, \rho}\right)$$

before burn and

$$P = f c_2 \rho T$$

during and after burn, where $0 \le f \le 1$ is the burn fraction. The specific energy is given by

$$\varepsilon = c_1\, T \quad ,$$

and at detonation time an initial specific energy of

$$\dot{\epsilon}_{burn} = c_4 c_5 \rho$$

is put into the material. Detonation time is determined by specifying the point of detonation and the detonation wave velocity. The parameters (c_1, c_2, c_4, c_5, and the detonation velocity) should not be chosen independently. The parameter c_5 is naturally taken to be ρ_0^{-1} and c_1 is chosen to give reasonable material temperatures. The other two parameters are determined self-consistently, given the known detonation velocity, to insure that the Chapman-Jouguet condition is satisfied. Failure to be consistent tends to cause the shock front and the detonation front to diverge when using a lighting-time model. Surprisingly, the default parameters in RAVEN, which were taken from another document that purports to model PBX-9404, were not consistent.[12] The parameter values used in the RAVEN simulation, which most closely match the case-motion velocity, are as follows: $c_1 = 861.6$ J kg^{-1} K^{-1}, $c_2 = 2,348$ J kg^{-1} K^{-1}, $c_4 = 3.009 \times 10^6$ J kg^{-1}, $c_5 = 5.464 \times 10^{-4}$ kg^{-1} m^3, and $v_{det} = 8,800$ m s^{-1}.

Results of the postshot RAVEN calculations are given in Figs. 21 through 25. Revised RAVEN calculations were done with 13 submodules divided among 3 modules rather than than 10 submodules in 1 module. This change allowed better resolution of the output end of the CN-III.
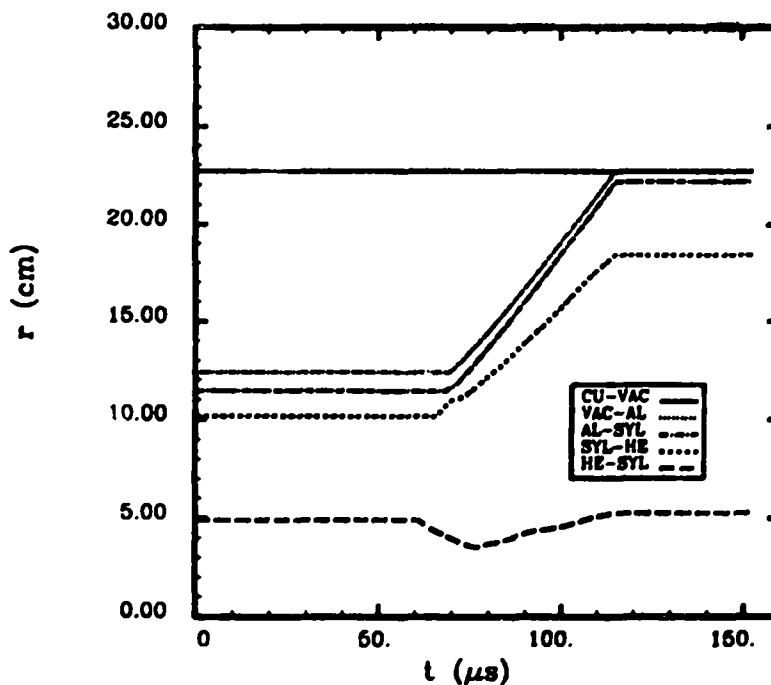

Fig. 21. Postshot calculated interface profiles of the input-end RAVEN module using 3.0-MA initial seed-current for the medium-current CN-III experiment. Calculations are done with multimodule RAVEN and scaled HE parameters.
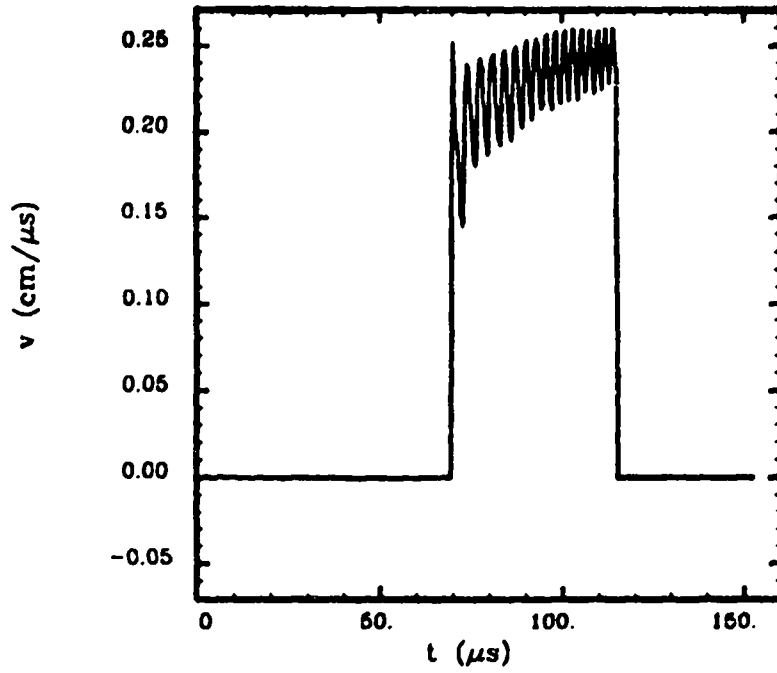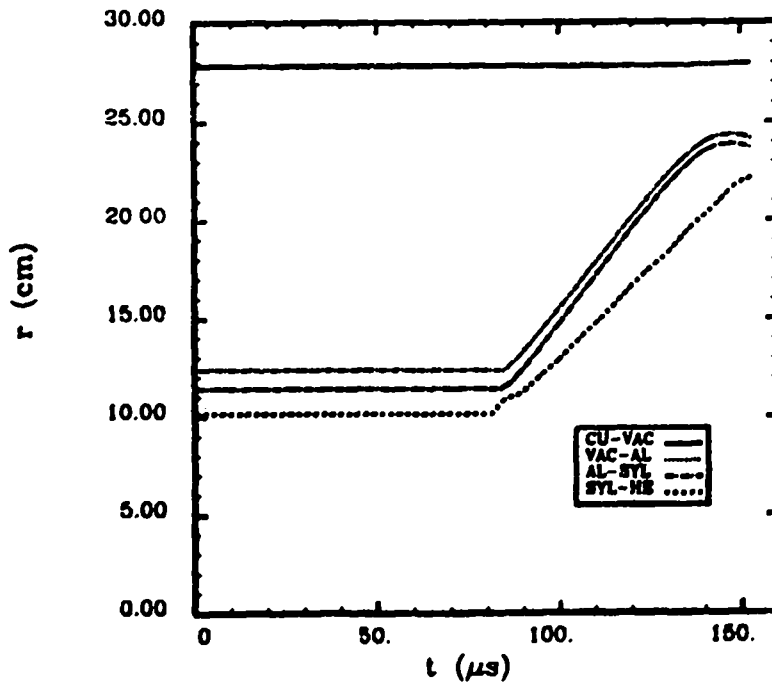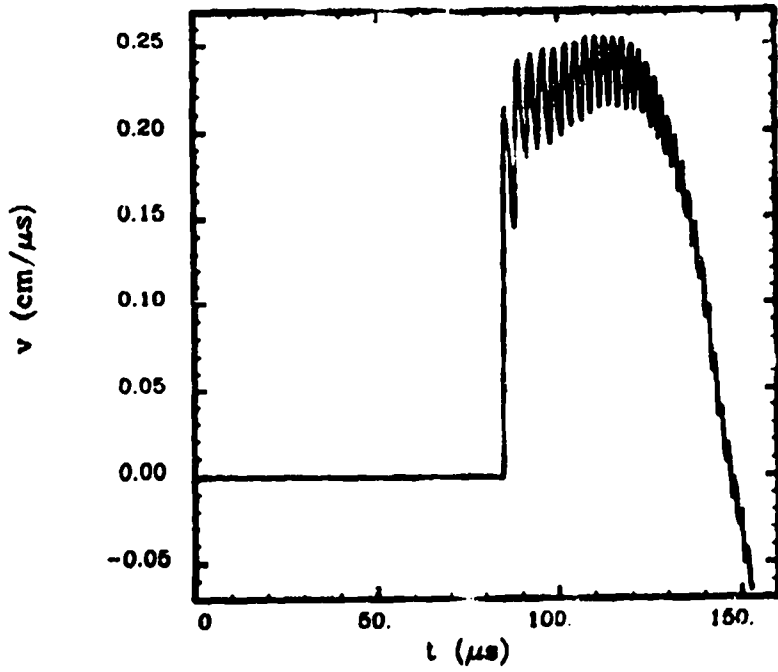
Fig. 22. Postshot calculated armature velocity of the input-end RAVEN module using 3.0-MA initial seed-current for the medium-current CN-III experiment. Calculations are done with multimodule RAVEN and scaled HE parameters.
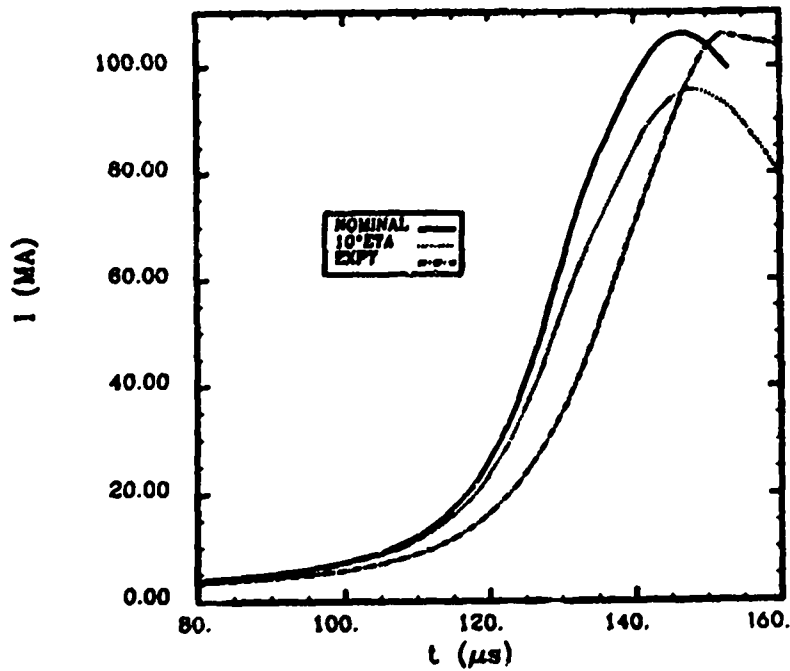

Fig. 23. Postshot calculated interface profiles of the output-end RAVEN module using 3.0-MA initial seed-current for the medium-current CN-III experiment. Calculations are done with multimodule RAVEN and scaled HE parameters.

31

Fig. 24. Postshot calculated armature velocity of the output-end RAVEN module using 3.0-MA initial seed-current for the medium-current CN-III experiment. Calculations are done with multimodule RAVEN and scaled HE parameters.

Fig. 25. Postshot calculated current waveform using 3.0-MA initial seed-current for the medium-current CN-III experiment. Calculations are done with multimodule RAVEN and scaled HE parameters.

A change was also made by using SESAME EOS 3718 for aluminum, though the difference for most quantities of interest is not significant. Interface profiles for the input end are given in Fig. 21, and the armature velocity at the input end is plotted in Fig. 22. The oscillations in the velocity are a direct result of the negative pressures in SESAME EOS 3718, which are included to mock up material strength at and below the melting temperature and near reference density. Similar plots for the output end are shown in Figs. 23 and 24. Using the scaled HE parameters, the postshot calculated peak current is 107 MA, and the current profile is given in Fig. 25. Also in Fig. 25 is a direct comparison with the experimental current and results from a calculation with a resistivity multiplier of 10 for the aluminum.

Designing, predicting, fielding, analyzing, and recalculating the medium-current CN-III experiment provided the groundwork necessary for assuring that the last CN-III experiment would meet the series goals. Two important conclusions were reached concerning FCG operation and modeling. First, the important quantity for modeling peak current in an FCG, in which the magnetic field stops the armature and leaves inductance within the generator volume, is armature kinetic energy. Variations in resistivities, EOS's, and initial current cause only small changes in the limiting current of the generator. For example, additional resistive losses in the generator are compensated by a greater compression ratio of the remaining flux, whereas a larger initial current stops the armature sooner, leaving more inductance in the generator. The net result is that the predicted final current is only a weak function of almost everything except the armature kinetic energy, as long as the final magnetic field is strong enough to stop the armature with inductance left in the generator. More specifically, the key variable is the kinetic energy of the portion of the armature that actually gets stopped. Second, the kinetic energy of the armature is unimportant for predicting peak current in an FCG unless the armature is significantly slowed down by the magnetic field. In the low-current-density case, calculated generator outputs like voltage and power can be easily rescaled to match experiment by using a measured velocity. Peak current is unaffected by this scaling. Calculated currents are, however, quite sensitive to EOS, resistivity, and zoning resolution. When generator gain is controlled by resistive losses, longer operating times, indirectly related to armature kinetic energy, can reduce calculated peak currents. This was verified by returning to calculations of the low-current test with the rescaled HE parameters. As a result, calculational uncertainties in the peak current are larger in the low-current-density regime than in the high-current-density regime. The exception to this rule arises from the fact that catastrophic generator failure, from causes such as armature breakup, glide-plane contact resistances, instabilities, arcing, etc., are harder to predict at higher-current densities when the generator is more heavily stressed.

VII. HIGH-CURRENT CN-III

A. Purpose

Two major goals were established for the last CN-III test. The first goal was to reach a peak current of 150 MA. Given a fixed stator radius, this goal could only be accomplished by challenging the conclusions of the first three tests. The results of calculations performed before and after the medium-current test, confirmed by the test itself, concluded that in its incarnation of Fig. 1, the CN-III is limited to ≤ 110 MA. Therefore, a redesign of the generator to add ≥ 50 MA of current was required. The second goal was to push the 1-MA/cm traditional limit hard enough to significantly exceed it or "break" the CN-III in the effort. The redesign of the CN-III was accomplished with RAVEN and the 2D Eulerian MHD code. Therefore, a third goal of the last CN-III test was to verify the calculated performance of the redesigned generator, which was based *solely* on codes that were benchmarked in the first three experiments.

B. CN-III Redesign and RAVEN Calculations

Based on the understanding gleaned from analysis of the medium-current test, one way to increase the final current of the CN-III would be to put more kinetic energy into the armature and then stop it with the magnetic field. Increasing the kinetic energy can be done by increasing the armature velocity while holding the mass constant, increasing the mass while holding the velocity constant, or some combination. Armature velocity is controlled by the strength of the HE shock and by the thickness of the armature. Since a more energetic HE was not available and thinning the armature would cut down its mass and weaken it, the decision to increase the mass and maintain the velocity was a natural one. This was done by adding 2.86 cm to the HE radius and expanding the armature radius by the same amount while keeping its thickness fixed. The result is a more massive armature that still travels about 0.23 cm/μs and a new CN-III that has $\sim$60 nH less inductance. This new CN-III would, therefore, have a realistic current gain of $\sim$50 rather than $\sim$70 in the low-current-density regime. In the high-current-density regime, the higher energy armature should produce a higher peak current. New RAVEN calculations of this bigger CN-III armature verified this conclusion and gives a generator with a current limit of $\sim$130 MA, which is indeed larger than the old limit of $\sim$110 MA, but is still short of the desired 150 MA.

Squeezing another 20+ MA out of the CN-III required stopping a larger fraction of the more-energetic armature without leaving too much additional inductance in the generator at peak current. This is accomplished by replacing the solid Falcon by another simultaneous section. This change should make very little difference in a current versus remaining generator inductance curve until only a few nanohenries remain in each generator. Significant resistive losses and armature stoppage do not begin until generator currents get large

and the inductance left in the generator is small. The dynamic armature profiles of the all-simultaneous and the propagating CN-III differ in a very important way near the end of their runs. With only a few nanohenries of inductance left in the two generators, a much larger fraction of the all-simultaneous armature is still active, than that of the propagating system. Furthermore, all of the active armature of the all-simultaneous CN-III is at a larger radius and hence experiences a smaller magnetic pressure than the portion of the propagating CN-III armature, which is less expanded but carries the same total current. In this way, an all-simultaneous CN-III is capable of converting a larger fraction of its total kinetic energy into electromagnetic energy and, therefore, produce a higher peak current even though more total energy is dissipated through resistive heating.

Calculations with RAVEN, using 13 submodules in 3 modules, predict that an all-simultaneous CN-III with an extra 2.86-cm-thick HE charge and a corresponding increase in armature diameter has a limiting current of $\sim$180 MA. Simulations with initial current loadings between 4.75 MA and 7.75 MA showed the expected weak dependence of the final current on EOS, resistivity, and initial current. Initial currents <4.75 MA are not sufficient to stop the armature, whereas initial currents >7.75 MA tend to stop the armature early in the run leaving too much inductance in the generator with a resulting drop-off in peak current. Based on these calculations, an initial current of 6.25 MA was chosen for the experiment. The preshot RAVEN prediction for the current is shown in Fig. 26. Three curves are presented in Fig. 26. The curve that peaks at $\sim$180 MA is derived from a calculation using the same scaled HE parameters, EOS's, and resistivities as in the postshot calculations of the medium-current experiment. The lower curve, which peaks at 160 MA, comes from an identical calculation except for the addition of a resistivity multiplier of 10 for the armature. The middle curve has a resistivity multiplier of 2. Given that the 180-MA calculation optimistically predicts a linear current density in excess of the 1-MA/cm limit, it was expected that the most probable final current in the last CN-III experiment would be 160 MA with a range between 150 and 180 MA. Interface profiles and armature velocities for the input and output ends of the CN-III from the 180-MA RAVEN calculation are displayed in Figs. 27 through 30. The armature velocity predicted by RAVEN for the last CN-III experiment is higher than that for the first three smaller armature experiments. Since the scaled HE parameters were normalized for the smaller diameter armature, an additional uncertainty was introduced for the last test.
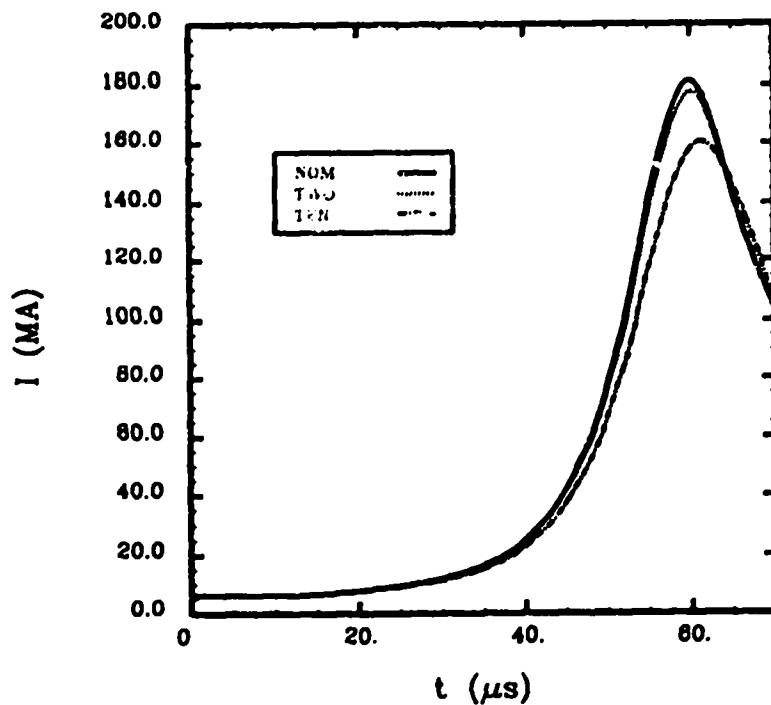
Fig. 26. Preshot calculated output current for the high-current CN-III experiment from multimodule RAVEN.
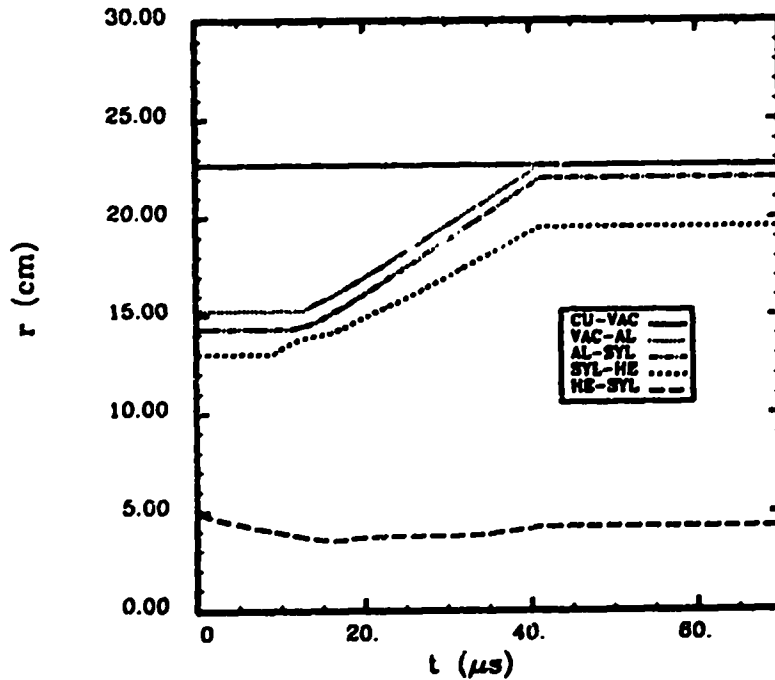

Fig. 27. Preshot calculated interface profiles of the input-end RAVEN module using 6.25-MA initial seed-current for the high-current CN-III experiment. Calculations are done with multimodule RAVEN, nominal resistivities, and scaled HE parameters.
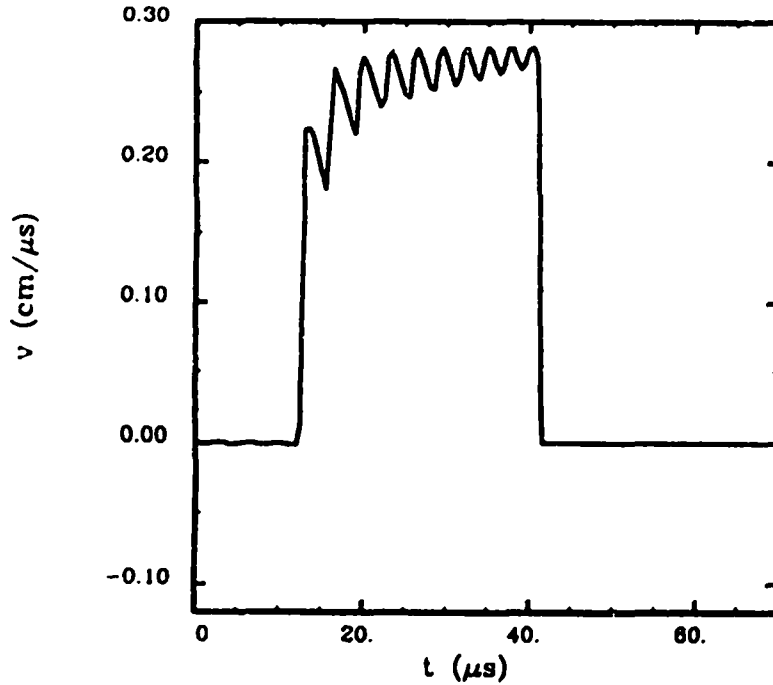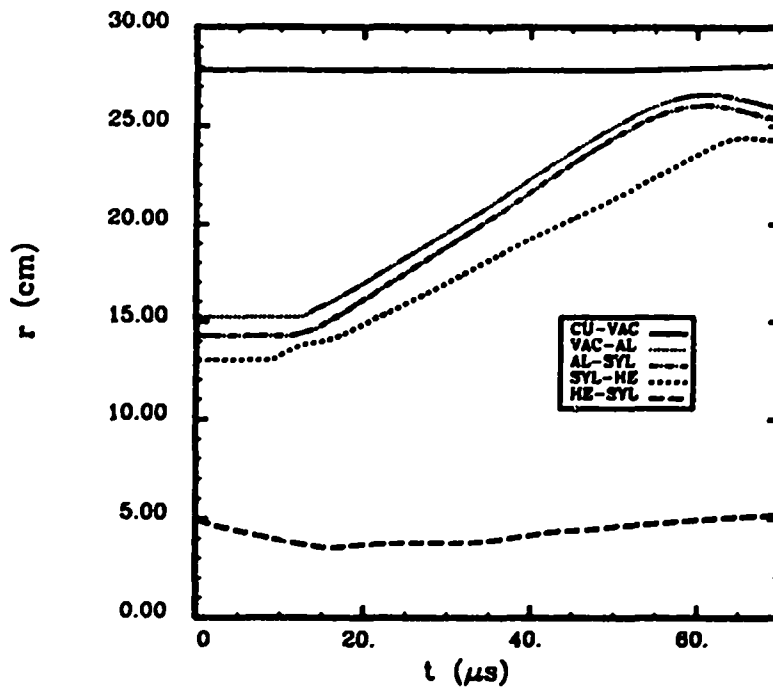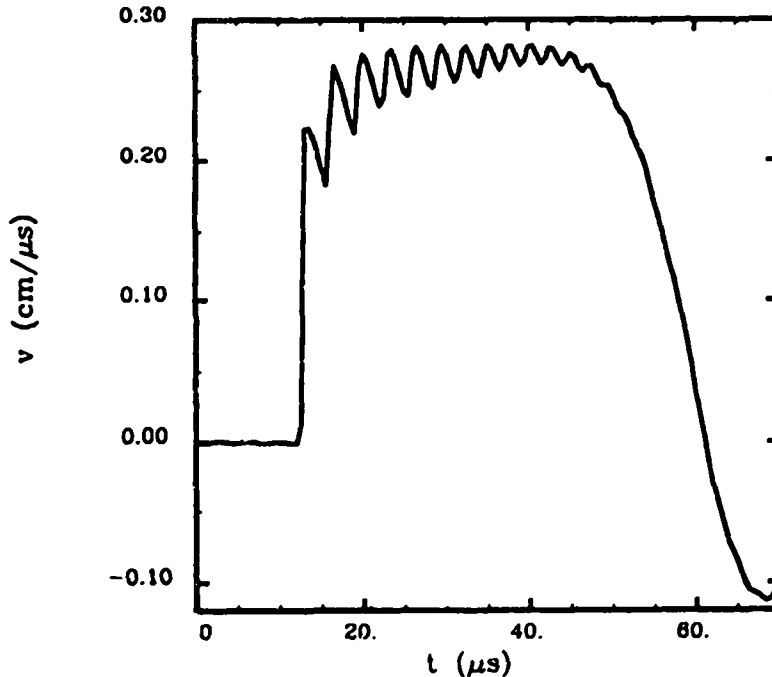
Fig. 28. Preshot calculated armature velocity of the input-end RAVEN module using 6.25-MA initial seed-current for the high-current CN-III experiment. Calculations are done with multimodule RAVEN, nominal resistivities, and scaled HE parameters.

Fig. 29. Preshot calculated interface profiles of the output-end RAVEN module using 6.25-MA initial seed-current for the high-current CN-III experiment. Calculations are done with multimodule RAVEN, nominal resistivities, and scaled HE parameters.

37

Fig. 30. Preshot calculated armature velocity of the output-end RAVEN module using 6.25-MA initial seed-current for the high-current CN-III experiment. Calculations are done with multimodule RAVEN, nominal resistivities, and scaled HE parameters.

C. Two-Dimensional Calculations and Redesign

Increasing the armature diameter and changing the HE design, reintroduced questions concerning glide-plane physics. Design of the glide planes was again constrained by the fact that the pieces were already cast and could only be remachined. It was decided that the axial distance between the glide-plane attach points, across both the armature and the stator, would be maintained. This change involved only a remachining of the glide planes to increase the convergence angle.

Calculations with the 2D Eulerian code, like the ones performed for the case-motion experiment, indicated that a 1.27-cm-thick propagating disk of HE needed to be added to the output end of the last Falcon module. The addition of this piece of HE smoothed the pressure profile in the armature between the end of the HE charge and the glide-plane attachment point. Without the propagating HE disk, the 2D code suggested that the armature might be thinned and severed, causing catastrophic failure of the CN-III.

For this last experiment, the 2D code was used, with MHD, to model the CN-III. The almost all-simultaneous armature, coupled with the Eulerian-to-Eulerian link capability, allowed adequate resolution of the armature throughout the generator run. The code was operated in an energy-based mode using analytic EOS's and resistivity models. The 2D predicted preshot current profile is given in Fig. 31. An interesting difference between the

38

RAVEN predictions and the 2D predictions is that even though both predict a 180-MA peak current, the 2D code does not show armature stoppage. The armature does slow down in the 2D calculations, but as the linear current density approaches the 1-MA/cm limit, the armature becomes more resistive and magnetic flux is lost rapidly through Joule heating of the armature. The difference between the two predictions is that RAVEN predicts that the armature will stop, leaving inductively stored energy in the generator, whereas the 2D code allows complete compression of the vacuum inductance but dissipates magnetic flux in heat of the armature instead. Both codes predict the same final flux in the 2-nH load and hence the same peak current. The truth almost certainly lies somewhere in between with an additional complication introduced by 3D perturbations, which are unavoidable and uncalculable by either code.

Fig. 31. Preshot calculated output current for the high-current CN-III experiment from the 2D Eulerian MHD code.

D. Experimental Results

The required initial current of 6.25 MA was too large to be delivered directly from the Firing Point 88 capacitor bank. Instead, a Mark IX helical FCG[13] was loaded to 260 kA from one module of the Firing Point 88 bank operating at 14.5 kV. The output of the Mark IX was input into the CN-III resulting in an initial load-current of 6.1 ± 0.1 MA. Mark IX output current is shown in Fig. 32. Output current from the CN-III was obtained from counter-rotating Rogowski loops located in the load ring. By using counter-rotating loops, some

noise cancellation is possible. The raw signal from the two loops, converted to MA/μs, is shown in Fig. 33, and the noise-canceled, integrated signal is given in Fig. 34. Peak current measured by the Rogowski loops is 153 ± 8 MA. Also, data from two different-wavelength, fiber-optic, Faraday rotation probes, both of which survived to the end of the generator run, gave peak currents of 153 MA and 160 MA. The time-dependent traces from these probes are displayed in Fig. 35. A B-field crystal located at the outer diameter of the load ring measured a magnetic field of 0.9 MG. Given the sum of the data collected, and comparing it with calculations, either the armature was stopped, broke apart, or became very resistive just before reaching a linear current density of 1 MA/cm.

VIII. SUMMARY AND CONCLUSIONS

The CN-III, advanced-FCG development series was successful, with all four experiments yielding good data. The last shot exceeded the 150-MA series goal with a final e-folding current risetime of less than 10 μs. The 1-MA/cm "rule-of-thumb" limit for the linear current density, which can be carried by an HE-driven moving conductor, was challenged and realized with the conclusion that this is a rule to be respected when designing HE-driven FCGs. Finally, two MHD codes were successfully benchmarked against data from all aspects of the four experiments.
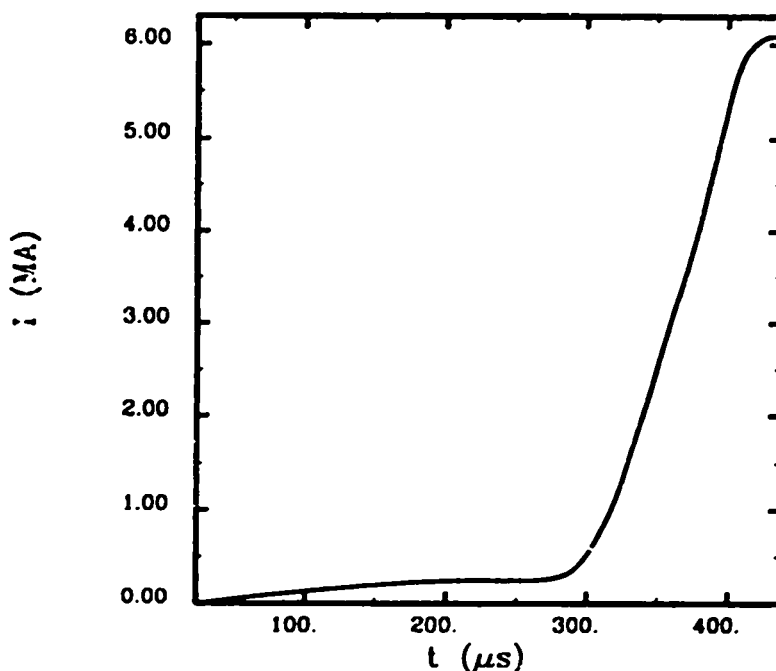

Fig. 32. Experimental trace of the Mark IX output current, which served as the seed-current for the high-current CN-III experiment. The curve is obtained by integrating a signal from a Rogowski loop located in the feed slot of the CN-III.
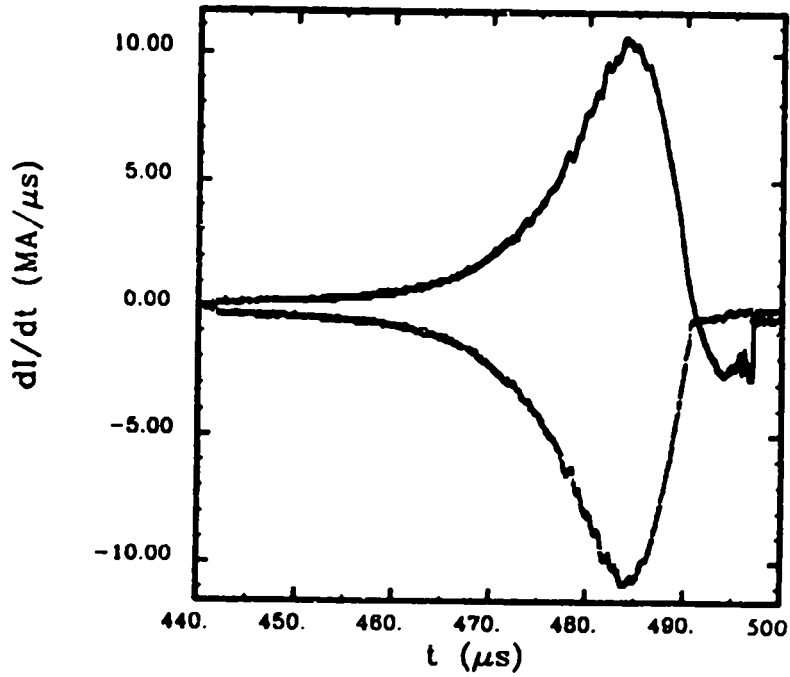
Fig. 33. Current derivative as measured by counter-rotating Rogowski loops in the load ring of the high-current CN-III.
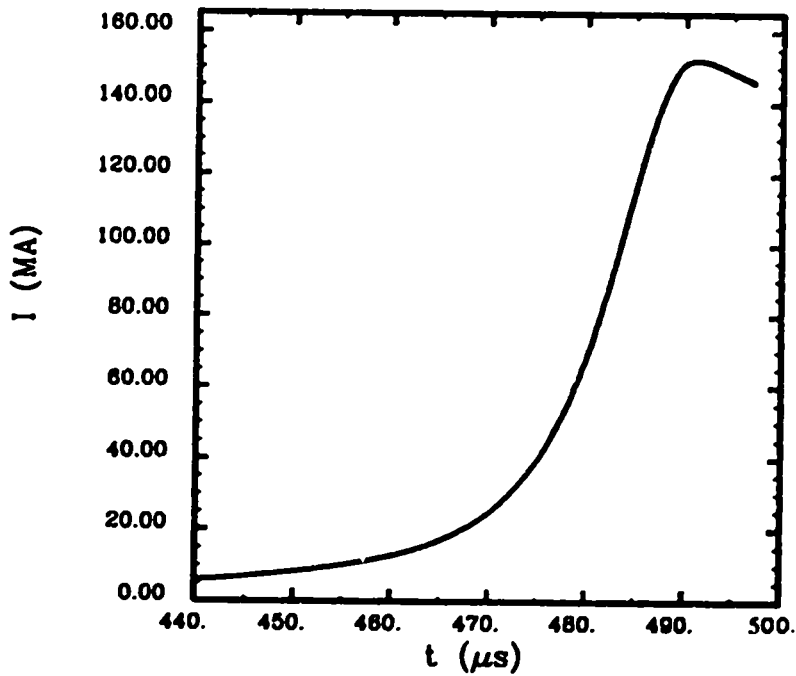

Fig. 34. Output current obtained by integrating the signal provided by counter-rotating Rogowski loops in the load ring of the high-current CN-III.
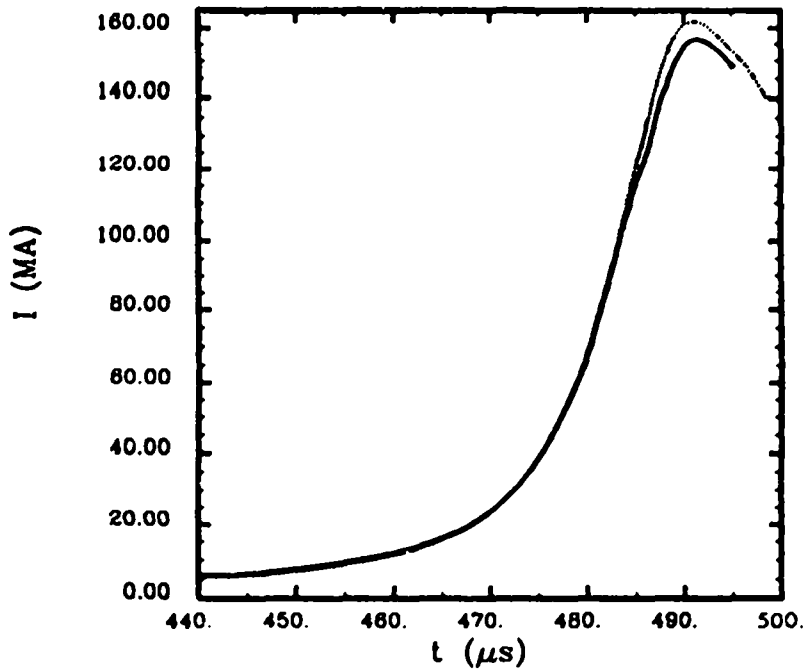
Fig. 35. Output current for the high-current CN-III as measured by fiber-optic, Faraday rotation probes.

With the verification of the 1-MA/cm law of HE-driven FCG design and the successful benchmarking of the codes, the design of fast-risetime, high-current, coaxial FCGs for various loads can be accomplished with fewer experimental development tests. Achieving higher currents requires larger diameter armatures. For example, it is unlikely that a 300-MA peak current can be produced by a generator of less than a 1-m diameter. This is consistent with recent reports of Soviet accomplishments using large disk FCGs,[4-7] and this insight makes interpretation of their results easier.[14] This series has demonstrated that higher efficiencies can be realized by substantially slowing the armature against the internal fields. However, the reliability of such generators driving active loads has not been thoroughly investigated. Design of new generators requires that a balance between risetime, peak current, flux loss, geometry, FCG inductance, HE conversion efficiency, HE mass, and total FCG weight and size be considered to achieve an optimal design for a given application.

IX. ACKNOWLEDGEMENTS

42

LANL's WX-3, provided outstanding support in the explosive assembly and quality assurance of these tests. James Griffin, retired from WX-3, made the Falcon initiation system possible through his personal perseverance. Finally, Kerry Sowder and David Torres contributed to these experiments as M-6 firing point supervisors above and beyond the call of duty.

REFERENCES

1. M. Sheppard, T. Oliphant, D. Weiss, and B. Freeman, "Multiple, Simultaneous, Coupled, One-Dimensional MHD Calculations for Modeling Two-Dimensional, Coaxial Flux-Compression Generators," presented at the *Seventeenth IEEE International Conference on Plasma Science*, paper 2C4, Oakland, CA (May 1990).

2. M. Sheppard, B. Freeman, and T. Oliphant, "Calculational Design of a Very High-Field Explosive Magnetic Flux Compression Generator," presented at the *Eighteenth IEEE International Conference on Plasma Science*, paper 2B8, Williamsburg, VA (June 1991).

3. B. Freeman, M. Sheppard, and C. M. Fowler, "Test Results of a Very High-Field Explosive Magnetic Flux Compression Generator," presented at the *Eighteenth IEEE International Conference on Plasma Science*, paper 2B7, Williamsburg, VA (June 1991).

4. A. Pavlovskii, R. Lyudaev, and B. Boyko, "Disk Magnetic Cumulation Generators Maximum Characteristics," in *Megagauss Fields and Pulsed Power Systems*, V. Titov and G. Shvetsov, Eds. (Nova Science, New York, 1990), pg. 327.

5. A. Pavlovskii, R. Lyudaev, B. Boyko, A. Boriskin, A. Kravchenko, V. Gurin, and V. Mamyshev, in *Megagauss Fields and Pulsed Power Systems*, V. Titov and G. Shvetsov, Eds. (Nova Science, New York, 1990), pg. 331.

6. V. Chernyshev, B. Grinevich, V. Vahrushev, and V. Mamyshev, "Scaling Image of ~90 MJ Explosive Magnetic Generators," in *Megagauss Fields and Pulsed Power Systems*, V. Titov and G. Shvetsov, Eds. (Nova Science, New York, 1990), pg. 347.

7. V. Demidov, A. Kraev, V. Mamyshev, A. Petrukhin, V. Pogorelov, V. Chernyshev, V. Shevtsov, and V. Shpagin, "Three-Module Disk Explosive Magnetic Generator," in *Megagauss Fields and Pulsed Power Systems*, V. Titov and G. Shvetsov, Eds. (Nova Science, New York, 1990), pg. 351.

8. C. M. Fowler, R. Caird, and W. Garn, "An Introduction to Explosive Magnetic Flux Compression Generators," Los Alamos Scientific Laboratory report LA-5890-MS (March 1975).

9. I. R. Lindemuth, J. H. Brownell, A. E. Greene, G. H. Nickel, T. A. Oliphant, and D. L. Weiss, "A Computational Model of Exploding Metallic Fuses for Multimegajoule Switching," *J. Appl. Phys.* 57, 4447 (1985).

10. R. M. More, Lawrence Livermore National Laboratory Report No. UCRL-84991 (March 1981).

11. Y. T. Lee and R. M. More, *Phys. Fluids* 27, 1273 (1984).

12. D. L. Johnson, "High Explosives Equation of State for MAGPIE," Air Force Weapons Lab Technical Note AFWL-DYS-TN-75-112 (1975).

13. C. M. Fowler and R. Caird, "The Mark IX Generator," in *Proceedings of the Seventh IEEE Pulsed Power Conference*, pg. 475, Monterey, CA (June 11-14, 1989).

14. M. G. Sheppard and B. L. Freeman, "Advanced Magnetic Flux Compression Generator Development Issues: A Comparison of Coaxial and Disk Generators," Los Alamos National Laboratory Memorandum X-10(8-90)14.